Bioactive Materials xxx (xxxx) xxx

Contents lists available at ScienceDirect

Bioactive Materials

journal homepage: www.keaipublishing.com/en/journals/bioactive-materials

Engineering biomolecular systems: Controlling the self-assembly of gelatin to form ultra-small bioactive nanomaterials

Dhananjay Suresh [a], Agasthya Suresh [a,b], Raghuraman Kannan [a,b,*]

[a] Department of Radiology, University of Missouri, Columbia, MO, 65212, United States
[b] Department of Bioengineering, University of Missouri, Columbia, MO, 65212, United States

ARTICLE INFO

Keywords:
Gelatin nanoparticle synthesis
Nanocomposite
Self-assembly
3D tumor spheroids
Ultra-small

ABSTRACT

The size of nanocarriers determines the biological property of the materials, especially as it relates to intratumoral distribution. Previous research has shown that sizes of 10–50 nm penetrate deep inside the tumor, resulting in better efficacy. On the other hand, studies have shown that gelatin exhibits excellent biological properties, including compatibility, degradability, and toxicity. Therefore, FDA approved gelatin as a safe material to use as an excipient in injectables. The bottleneck is the nonexistence of smaller-sized gelatin nanoparticles (GNPs) to realize the full potential of these biomaterials. Yet, GNPs with sizes of less than 50 nm have not been reported; the synthetic strategy reported in the literature uses "uncontrolled crosslinking coupled with nanoprecipitation", resulting in larger particle size. We have developed a new method to self-assemble gelatin strands by using an anionic, phosphate-based crosslinker and controlled precipitation. The method we developed produced ultra-small gelatin nanoparticles (G^X) of size 10 nm with a high degree of reproducibility, and it was characterized using dynamic light scattering (DLS), Energy-dispersive X-ray spectroscopy (EDS), High-resolution transmission, and scanning electron microscopy (HR-TEM/STEM). We also explored G^X as a bioactive platform to encapsulate imaging and therapy agents within the cavity. Interestingly, we were able to encapsulate 2 nm size gold nanoparticles within the void of G^X. The versatile nature of the G^X particles was further demonstrated by surface functionalizing with larger size gelatin nanoparticles to form core-satellite nanocomposites. Additionally, we studied the tumor penetrability of dye-tagged 10, 50, and 200 nm gelatin nanoparticles. The study showed that smaller size gelatin nanoparticles penetrate deeper tumor regions than larger particles. In general, G^X was efficient in penetrating the inner region of the spheroids. The results demonstrate the potential capabilities of ultra-small G^X nanoparticles for multi-staged payload delivery, diagnostics, and cancer therapy.

1. Introduction

Bioactive gelatin has gained significant prominence in recent years due to its application in various medical fields ranging from tissue regeneration to cancer therapy [1–4]. It is biodegradable, biocompatible, non-immunogenic, and approved by FDA as a safe pharmaceutical excipient; additionally, it is easily sterilizable and has a low degree of antigenicity [5]. By converting gelatin into nanoparticles, gelatin gained greater utility in medicine, especially as a drug delivery agent for a vast array of diseases. There are a plethora of examples showing that gelatin nanoparticles (GNPs) as delivery agents show multi-fold improvement in therapy [6–8]. For example, GNPs are used for delivering methotrexate, tirapazamine, bone morphogenic protein-2 or angiogenic basic fibroblast growth factor (bFGF) *in vivo* [9–12]. Despite GNPs' great potential, their large size (>200 nm) prevented their full utilization and hinder them in advancing for human use. When it comes to cancer, for instance, smaller nanoparticles have a better therapeutic response than larger ones [13,14]. It is because larger particles cannot penetrate deep into tumors to impart long-lasting therapeutic benefits [15]. For example, the FDA-approved Doxil and Abraxane, showed only modest therapeutic benefits due to their larger sizes (>100 nm) [16]. Indeed, several systematic studies concluded that the size of the nanoparticles governs the transport and diffusion within tumor [13,17–20]. Liang and colleagues evaluated the tumor penetrability of gold nanoparticles of 50 and 100 nm and found that the smaller particles penetrated deeper into the tumor [21]. Of relevance to the present study, Wong and coworkers

Peer review under responsibility of KeAi Communications Co., Ltd.
* Corresponding author. Departments of Radiology and Bioengineering, University of Missouri, Columbia, MO, 65212, United States.
E-mail address: kannanr@health.missouri.edu (R. Kannan).

https://doi.org/10.1016/j.bioactmat.2022.02.035
Received 20 December 2021; Received in revised form 11 February 2022; Accepted 28 February 2022

have shown GNPs encapsulated with quantum dots (QD) exhibit size-dependent permeability, with smaller size QD finding a way into deep tumors when gelatin is digested by matrix metalloproteinases [22]. Similarly, Gao and coworkers synthesized MMP-2 protein shrinkable GNPs tethered with AuNP-Doxorubicin conjugate to reach a deep tumor region resulting in increased efficacy [23]. Although research works showed that smaller particles encapsulated within GNPs might reach deep tumors, no studies have been performed to determine whether GNPs would do the same. The data is rare because smaller GNPs hitherto unavailable. Therefore, it is evident that developing a methodology to synthesize smaller sized GNPs and understanding their tumor penetrability are of paramount importance. Such a study will essentially fill the void in this area and will help us to evaluate whether tumor penetrability will be affected by the size of GNPs. Indeed, the results from the investigation would shed light on recognizing GNPs fullest potential and enable the researchers to develop a roadmap for their future use in humans.

GNPs are traditionally synthesized using the desolvation technique, wherein an organic solvent (antisolvent) is added to gelatin dissolved in 50 °C water (gel sol) to form clustered proteins which are further crosslinked with glutaraldehyde to obtain rigid particles of size 200–300 nm [24]. Researchers have altered pH, temperature, and crosslinker to synthesize smaller GNPs. But these attempts thus far have generated GNPs larger than 100 nm, and particles smaller than that have not been obtained [25–27]. In an interesting study, researchers tried to shrink GNPs to 100 nm using a freeze-thaw method [28]. Taken together, the synthesis of GNPs of smaller sizes (>20 nm) is a significant challenge and remain unsolved. To overcome this challenge, we developed a new method wherein we protonated the " $= NH_2$" groups on the backbone of gelatin and bonded them through ionic crosslinkers. By using shorter crosslinkers, we could preferentially allow ammonium ions within the same strand to attach to one another than in to different strands. Using this technique, we synthesized 10 nm-sized gelatin nanoparticles (G^X) and demonstrated its versatility by encapsulating therapeutic and imaging agents. We also used G^X as a platform to encapsulate smaller size gold nanoparticles, and multi-sized single nanoparticles (i.e., 200 nm GNPs surface attached with multiple G^X). Furthermore, we systematically assessed the deep tumor penetration of 10 (G^X), 50 (G^L), and 200 (G^{CC}) nm gelatin nanoparticles using 3D tumor spheroids. To the best of our knowledge, this is the first report on the synthesis of smaller (10 nm) sized gelatin nanoparticles. In this report, we present detailed synthesis and characterization of smaller sized GNPs, its encapsulation capability, and tumor spheroid penetrability.

2. Experimental section

2.1. Materials

Gelatin (Bloom type-A; CAS No. 9000-70-8), Sodium tripolyphosphate (TPP; CAS No. 7758-29-4), Rhodamine-B (CAS No. 81-88-9), Cisplatin dichloride (CAS No. 15663-27-1), sodium borohydride (CAS No. 16940-66-2), dithiolated diethylenetriamine pentaacetic acid (DTDTPA), gold (III) chloride hydrate (CAS No. 27988-77-8) and glutaraldehyde (CAS No. 111-30-8) were purchased from Sigma-Aldrich (USA). Sterile ultraclean distilled water (Cat No. 10-977-015), sodium hydroxide (NaOH; CAS No. 1310-73-2), hydrochloric acid (HCl; CAS No. 7647-01-0), 200-proof ethanol (CAS No. 64-17-5), acetone (CAS No. 67-64-1), sodium chloride (NaCl; CAS No. 7647-14-5), sucrose (CAS No. 57-50-1), paraformaldehyde (PFA; Cat. No. 50-980-486), RPMI-media (Cat. No. A1049101) and fetal bovine serum (FBS; Cat. No. 26-140-079) were purchased from Thermo Fisher Scientific (USA). HS-PEG-OMe (Cat. No. 12750-40) was purchased from RAPP Polymere (Germany) and HS-PEG-COOH (Cat. No. CM-PEG–SH–2000) was purchased from Laysan Bio (USA). Doxorubicin (CAS No. 25316-40-9) was purchased from LC Laboratories (USA). Cy5 NHS ester (Cat. No. 23020) was purchased from Lumiprobe (USA). Iodixanol (Visipaque ®; Cat. No. 00407222317) was obtained from GE Healthcare (USA).

2.2. Instrumentation

Automated liquid pipetting was performed on a single channel INTEGRA pipette. pH measurements were performed using a Mettler Toledo pH-meter. Controlled addition of solvents was achieved using a KDS-200 Syringe pump. Sonication was performed on a Branson Bransonic® M Mechanical Ultrasonic Bath 3800. Spheroids were imaged on a Leica TCS SP8 MP inverted spectral confocal microscope with tunable white light laser (470–670 nm) and with Mai Tai DeepSee multiphoton laser tunable to 680–1060 nm equipped with a two-channel time-correlated single-photon counting unit from PicoQuant, and two non-descanned HyD-RLD detectors for fluorescence lifetime imaging microscopy (FLIM). Hydrodynamic size and zeta potential was measured (by dynamic light scattering and laser doppler velocimetry techniques) on a Zetasizer Nano-ZS (Malvern Panalytical Ltd). Absorbance and fluorescence spectroscopy were performed on a BioTek Synergy H1 and Cytation-3 multi-mode microplate reader respectively. HR-TEM imaging was performed on a FEI Tecnai F30 twin microscope equipped with 300 kV field emission gun (FEG) high resolution TEM/STEM. The electron microscopy imaging point resolution was 0.24 nm with a Magnification range of 58x – 800 Kx in TEM mode. STEM-EDS was performed on a FEI Tecnai F30 twin equipped with a Bruker Energy Dispersive X-ray spectrometer (QUANTAX 400-STEM with XFlash®6 at an energy resolution <129 eV at MnKα). STEM imaging was performed using a FEI Quanta 600 FEG Environmental Scanning Electron Microscope (ESEM) equipped with a Schottky Field Emitter (thermal FEG), with an accelerating voltage from 200 eV to 30 keV with probe currents of 4.5 micro-amps.

2.3. Synthesis of G^X

To synthesize 10 nm gelatin nanoparticles (G^X), a modified *two-step* desolvation procedure was developed. In a 10 mL beaker, 3 mL of distilled water was heated (55 °C) and gelatin (125 mg) was slowly added and stirred (800 RPM) until a homogeneous gelatin sol (gel sol) was formed (~1 h). To this gel sol, acetone (6.5 mL) was rapidly added and stirred (900 RPM) for 30 s to precipitate high molecular weight (M.W.) fraction of gelatin (*first desolvation step*). The supernatant containing low M.W. gelatin was removed, and the residue was washed with water (1X, 5 mL) and used for the next step. To the residue, 3 mL of water was added and heated to form a gel sol (55 °C; 800 RPM; 2 h). Subsequently, the gel sol was acidified to pH 2.75 (1 M HCl) and transferred to a 25 mL round-bottom flask (RBF). The RBF was heated in an oil bath (65 °C; 900 RPM; 20 min). Independently, a stock-solution of tripolyphosphate (TPP; 0.5% w/v in water) was prepared. 10 μL of TPP stock solution was pipetted and added to 190 μL ethanol (vortex mixed); this solution was added dropwise to the RBF at rate of 10 mLh^{-1} using an automated pipette fixed with a 10 μL pipette tip. The reaction was stirred for 30 min. During this time, we prepared nanoprecipitant solution (0.01% TPP) by mixing 200 μL of TPP stock-solution with ethanol:acetone mixture (EtOH:Me_2CO 1:1 v/v). Next, we added the nanoprecipitant solution dropwise to the RBF at 25 mLh^{-1} using an automated syringe pump (10 mL syringe fitted with a 15 mm acetone-resistant tube tipped with a 22 g needle). The solution changed from transparent to a whitish colloid (~10 mL of nanoprecipitant) after which the addition was stopped, and the solution was stirred at 65 °C for 18 h (*second desolvation step*). The solution was cooled (25 °C; 1 h) and filtered through a 0.45 μm and a 0.22 μm sterile filter. The filtered solution was then reheated (70 °C; 15 min; Fig. S11), and quickly added into water (25 °C; 3x volume; 700 RPM) and left undisturbed for 72 h at room temperature (RT). After that, the dense irreversible gel that settled at the bottom was discarded. The supernatant was decanted and purified using sucrose density centrifugation (SDC; Order: bottom-50%, 20%, 10%, 5%, 2%, top-reaction solution) to obtain nanoparticles. The 5% fraction was then isolated and dialyzed (10 kDa) in water for 72 h (Fig. S12). The dry

weight of the G^X per batch was 7–10 mg and the purified nanoparticles could be stored as an aqueous solution at 25 °C.

2.4. Synthesis of G^L

To synthesize 50 nm gelatin nanoparticles (G^L), a modified two-step desolvation procedure was used [29]. Briefly, distilled water (5 mL) was heated in a 25 mL beaker (50 °C; 800 RPM). Gelatin powder (250 mg) was slowly added to the hot water to avoid clumps and stirred until a homogenous gelatin sol was formed (~1 h). Next, acetone (12 mL) was rapidly added to the gel sol (900 RPM) and stirred for 30 s to precipitate high M.W. fraction of gelatin. The supernatant containing low M.W. fraction was removed using a pipette and the precipitate was washed once with water (5 mL). Water (5 mL) was added to the beaker followed by gently loosening the precipitate using a pipette tip. The precipitate was then heated to form a gel sol again (50 °C; 800 RPM; 2 h). After 2 h, the homogenous gel sol was acidified to pH 2.75 (1 M HCl) and the solution was transferred to a 50 mL round-bottom flask (RBF) in an oil bath (55 °C; 900 RPM; 20 min). An ethanol:acetone mixture (1:10 v/v) was then added dropwise to the RBF at 50 mLh^{-1} using an automated syringe pump (10 mL syringe fitted with a 15 mm acetone-resistant tube tipped with a 21 g needle) until a whitish colloid formed. Separately, tripolyphosphate (TPP; 0.5% w/v in water; 1 mL) was vortexed mixed with ethanol (1 mL). The TPP solution was then added dropwise to the RBF at 10 mLh^{-1} using an automated pipette fixed with a 10 μL pipette tip until the solution turned to a slight off-white color. Glutaraldehyde (10 μL; 25% v/v) mixed with ethanol (190 μL) was added dropwise and the reaction was stirred (800 RPM; 55 °C) until 18 h. After 18 h, solution was cooled (25 °C; 1 h) and filtered through a 0.45 μm and a 0.22 μm sterile filter and centrifuged to collect the pellet (15,000 g, 15 min). Pellet was resuspended in water using sonication and washed two times (15,000 g, 15 min). The residue was dried under vacuum to obtain ~20 mg of G^L powder (per batch). This procedure showed mediocre reproducibility, as 1 in 6 batches yielded the anticipated size distribution. The final nanoparticle solution was stored as an aqueous solution at 25 °C.

2.5. Synthesis of G^{CC}

To synthesize 200 nm gelatin nanoparticles (G^{CC}), we utilized a previously published two-step desolvation procedure [8]. Briefly, distilled water (11 mL) was heated in a 100 mL beaker (50 °C; 800 RPM). Gelatin powder (500 mg) was slowly added to the heated water to avoid clumps and stirred until a homogenous gelatin sol was formed (~1 h). Next, acetone (20 mL) was rapidly added to the gel sol (900 RPM) and stirred for 30 s to precipitate high M.W. solid fraction of gelatin. The solution containing low M.W. fraction was removed using a pipette and the precipitate was washed once with water (5 mL). Water (11 mL) was added to the beaker followed by gently loosening the precipitate using a pipette tip. The precipitate was then allowed to form a gel sol again (50 °C; 800 RPM; 2 h). After 2 h, the homogenous gel sol was acidified to pH 2.75 (1 M HCl) and the solution was transferred to a 100 mL round-bottom flask (RBF) in an oil bath (50 °C; 800 RPM; 10 min). 100% Acetone was then added dropwise to the RBF at 100 mLh^{-1} using an automated syringe pump (10 mL syringe fitted with a 15 mm acetone-resistant tube) until a whitish colloid formed (800 RPM; 10 min). Next, glutaraldehyde (200 μL; 25% v/v) was added dropwise and the reaction was stirred (800 RPM; 50 °C) until 18 h. After 18 h, solution was cooled (25 °C; 1 h) and centrifuged to collect the pellet. Pellet was resuspended in water using sonication and washed four times (20,000 g, 20 min) and the final resuspension in water was filtered through a 0.45 μm sterile filter. The procedure presented above yielded ~200 mg of dry G^{CC} powder per batch, however the nanoparticles were stored as an aqueous solution at 4 °C.

2.6. Synthesis of GNP-dye conjugates

To tag G^X, G^L, or G^{CC} with fluorescent dye (Rhodamine-B; RhB or Cyanine-5 NHS ester; Cy5), we developed the following protocol. A 20 mL glass vial was charged with nanoparticle (10 mg). The amount of NHS ester required for the reaction was calculated as per manufacturer's protocol. The dye solution (2 mg/mL in water) was added dropwise to the nanoparticle with continuous stirring (800 RPM; 18 h; 25 °C). In the case of NHS ester, the pH of the solution was adjusted to 8.2 (1 M NaOH) for efficient conjugation. After 18 h, G^X construct was subjected to dialysis in water for (96 h); whereas G^L and G^{CC} were purified by centrifugation technique (10,000 g for 10 min). Purified nanoconstructs GNP-RhB or GNP-Cy5 were stored at 25 °C.

2.7. Encapsulation of drugs or contrast agent in G^X

We optimized the following protocol for encapsulating doxorubicin (DOX), cisplatin (CP) or iodixanol (IO) in G^X. We followed the steps as described in Section 2.3 (see ES) till first desolvation. To the gel sol obtained, we added dropwise the following solution: 5 mg of DOX (in water), 5 mg CP (in 0.9% NaCl solution), or 10 mg of IO solution. After the addition, we continued the steps as described in Section 2.3 (see ES). The product was purified by either dialysis or centrifugation techniques. Purified conjugates G^X (DOX), G^X (CP), or G^X (IO) were stored at 25 °C.

2.8. Synthesis of G^X(Au) hybrid nanocomposite

For synthesizing multi-dimensional hybrid materials, we used five different gold nanoparticles, including 2 nm AuNP coated with DTDTPA or HS-PEG-COOH (M.W. 2000); naked 2 nm AuNP generated using $NaBH_4$ or THPC; and 10 nm citrate stabilized AuNPs. To encapsulate or surface attach gold nanoparticles of various sizes, 1 mg of AuNP in water was added dropwise to the gel sol after the first desolvation step (section 2.3). The gel sol was stirred for an hour and the solution was then acidified to pH 2.75. Subsequently, tripolyphosphate (TPP; 0.5% w/v in water; 10 μL mixed with 190 μL ethanol) was added to the acidified gel sol and the solution was stirred for an additional 30 min. Next, tripolyphosphate (TPP; 0.5% w/v in water; 200 μL) was vortexed mixed with an ethanol:acetone mixture (1:1 v/v; 0.01% TPP) and added dropwise to the RBF at 25 mLh^{-1} until the solution color changed from red/brown to a whitish-red colloid. The final nanoparticle solutions for G^X (AuNP) were stored at 25 °C.

2.9. Synthesis of G^{CC}-G^X core-satellite hybrid nanocomposite

To synthesize G^{CC} particles with G^X satellites, we used the purified G^X reaction-solution (filtered through a 0.2 μm filter). This solution was heated (65 °C) and a mixture containing TPP (50 μL; 0.5% w/v), glutaraldehyde (5–10 μL; 25% w/v) and HS-PEG-OMe (0.1 mg; M.W. 750) diluted in 1 mL of Ethanol was consecutively added and stirred for 72 h. The reaction mixture turned into a milky-solution indicating the formation of G^{CC}-G^Xsat hybrid particles. Final nanoparticle solutions were stored at 25 °C.

2.10. Dynamic light scattering (DLS)

Particle sizes were measured using dynamic light scattering (DLS) technique. Measurements were performed on a Zetasizer rated for 0.3 nm to 10 μm, using a 633 nm He–Ne laser source with a backscattering angle (NIBS) of 173°. Following general procedure was used: ~0.05 mg/mL GNP in water was used for the measurement. 800 μL of the GNP solution was pipetted, sonicated for 10 s and vortexed before adding into a low-volume cuvette. In the instrument, for the sample parameters, the material was selected as "protein" with a refractive index of $n = 1.45$, solvent was selected as water and the temperature was equilibrated to 25 °C. High-resolution measurements were performed in triplicates

(each measurement performed using 3 runs, 10 s each). The data analysis was performed on the Zetasizer software suite (ver 7.13), and the particle size data values were exported to Excel for plotting.

2.11. Zeta potential measurement

To monitor particle surface charge, laser Doppler microelectrophoresis technique using a non-invasive backscatter technology was used. Measurements of the surface charge at slipping planes (zeta potential) were determined on a Zetasizer using a 633 nm He–Ne laser source for conducting electrophoresis light scattering (ELS). Briefly, a 0.05 mg/mL GNP solution in water was prepared and 800 μL of this solution was sonicated (10 s), vortex mixed (5 s) and added into a DTS-1070 Zeta-measurement cell. For the sample parameters, we selected: material as "protein", Debye-Huckel approximation, solvent as "water", and the temperature was equilibrated to 25 °C. All measurements were performed in triplicates (each measurement performed using 10 runs). The data analysis was performed on the Zetasizer software suite (ver 7.13), and the zeta potential data values were exported to Excel for plotting.

2.12. High-resolution transmission electron microscopy (HR-TEM)

To image GNPs, high-resolution transmission electron microscopy (HR-TEM) was used. For this purpose, GNP stock solution (40 μL) was rapidly vortex-mixed in water (200 μL). The solution was then sonicated (5 s) and 8 μL was dropped on a 200-mesh carbon-coated copper grid. The drop was then air-dried (40 °C; 10 min and additional 25 °C; 2 h). The air-dried grids were then inserted into the HR-TEM using a single-sample single-tilt holder and imaged at 100 kV. Beam alignment (pivot point X and Y; shift and rotation center), coma-free beam alignment, and sigmator-alignment (condenser and objective) were performed at both low (<10 μm × 10 μm) and high (<100 nm × 100 nm) magnification prior to image acquisition. At 200 kV, particle disintegration was observed for long beam exposures (>1 min). Images were taken using a 1–0.5 s exposure and converted to TIFF using Gatan software.

2.13. Energy dispersive spectroscopy (EDS)

To detect elemental composition in G^X (CP) or G^X (IO), Scanning transmission electron microscopy – Energy-dispersive X-ray spectroscopy (STEM-EDS) was used. To perform measurements, carbon-coated copper grids with air-dried nanoparticles were inserted using a single-sample low-background double-tilt holder. After STEM alignment, STEM microscopy was performed at 200 kV in high angle annular dark field (HAADF) imaging mode. The STEM-EDS map acquisitions were then performed using a 30 mm^2 active area Bruker Silicon Drift Detector with a super light element window. Final spectral plots were then collected and saved using Bruker ESPIRIT software.

2.14. Scanning transmission electron microscopy (STEM)

To image GNPs, scanning transmission electron microscopy (STEM) was used. Briefly carbon-coated copper grids with air-dried nanoparticles were inserted using a multi-sample stage and imaged between 5 and 20 kV using the STEM detector. Images were processed using Gatan software.

2.15. Image analysis and volume reconstruction

To predict the three-dimensional (3D) structure of G^X nanoparticles, 3D topography was inferred from the TEM images and iterative 3D volume-models were prepared. Briefly, the TEM images were converted to 32-bit and processed for background subtraction, contrast enhancement, distance map to distance ridge mapping, and Euclidean distance transformation. These steps allowed the de-noising and selective computation of pixel intensities to visualize distance. Further the distance maps were processed using ImageJ Process-plugin to calculate the maximum 3D points to refine local thickness. Subsequently, the maximum values were used to build 3D surface plots to analyze surface topography of the TEM images. Using a 3-D builder, the topography was approximated to a block and duplicated along the z-axis to visualize the complete structure. Using visual cues of the vertexes and pore locations, several representative 3D models were generated using 3-D builder. Each of these models were rotated and several projected planes were captured, emulating a two-dimensional (2D) image. The emulated 2D images were processed through similar distance mapping and 3D surface plots were created. The predicted 3D surface plots were matched with the observations to select approximate structures that represent G^X. Final maps were saved as TIFF using Fiji (ImageJ2) (NIH) [30].

2.16. 3D spheroid assay

To perform the spheroid penetration assay, NCI-ADR-RES or A549 cell lines (90% confluency) were used. Briefly, three hundred A549 or NCI-ADR-RES cells were suspended in 200 μL of complete medium (RPMI 1640 + 10% FBS) and seeded into a Corning 96-well ultralow attachment microplate (Corning 4520), followed by centrifugation (200 g; 30 s; 25 °C). The plate was then incubated at 37 °C; 5% CO_2 for 5 days to allow the formation of 3D spheroids. The spheroids were washed twice with serum free media and treated with nanoconstructs (0.4 mg/mL; 6 h for segmentation analysis and 14 h for 3D reconstruction study; 37 °C). The treated spheroids were washed thrice with 1X DPBS and fixed in 2% buffered PFA (14 h for segmentation analysis and 2 h for 3D reconstruction study). Fixed spheroids were washed thrice with 1X DPBS and transferred onto confocal dishes for imaging using confocal fluorescence microscopy.

2.17. Confocal fluorescence microscopy (CFM)

To acquire fluorescence signal, spheroids in confocal dishes were imaged using a Leica TCS SP8 Confocal microscope using the excitation/emission parameters of RhB (554/564–644 nm) and Cy5 (647/655–705 nm). We used the following settings: Frame Average 1, Line Average 3, Frame Accumulation 1, Line Accumulation 1, with Linear Z Compensation. Z-sections at spheroid depths of 10, 20, 30, 40 and 50 μm were analyzed to study penetration ability of the constructs. Spheroid segmentation was carried out using the *SpheroidJ* plugin with Fiji (ImageJ2) [30,31]. The inner region of each section was defined by 2/3rd of the radius. Mean fluorescence intensity of the inner and outer region of each section was calculated using Fiji. 3D reconstruction of spheroids was performed using z-scan stacking and rotated along the x-axis for visualization, using Leica Application Suite X software (ver. No. 3.7.4.23, 463).

2.18. Statistical analysis

All data was collected in triplicates and averaged, unless indicated. Data was expressed as Mean ± Standard error of the mean. Graphing and statistical analysis was performed on Excel (Microsoft, USA) or Prism software (GraphPad, San Diego, CA, USA).

3. Results and discussion

3.1. Synthesis and characterization of G^X

The 200 nm Gelatin nanoparticles (G^{CC}) are prepared using a two-step desolvation process, as previously described (see experimental section; ES) [8,29,32,33]. The first step involves breaking the bonds in gelatin by heat and then separating the low and high molecular weight fractions. The next step involves the acidification of the high molecular weight fraction solution to protonate the amines in the gelatin backbone

to form ammonium ions. These cationic fragments induce repulsion between gelatin units to keep them apart [34]. Addition of antisolvent to this solution, induces precipitation to form gelatin nanoparticles of size ~200 nm. It is evident that the acidification step controls the phase behavior of gelatin sol and allows homogenous nanoprecipitation by displacing water molecules between units [34,35]. The individual units are clustered together with high degree of randomness; therefore, the nanoprecipitation step always results in larger size gelatin clusters [29,32]. We hypothesized that if the positively charged gelatin strands are arranged in a systematic fashion, then the desolvation step would induce smaller non-random clusters. One way to develop an ordered arrangement is to directionally connect the ammonium ions using an anionic crosslinker. These molecules should be coordinatively unsaturated, so they can serve as a nucleus to self-assemble with other units to form a smaller size nanoparticle. Using this synthetic approach, we could achieve the following crucial progress: (i) facilitate the intramolecular interaction of gelatin units using a polyanion that bridges an ionic link between the charged cationic amine groups of two individual polymer units (Figs. 1 and S1a), and (ii) slow the rate of nanoprecipitation by rationale choice of antisolvents with different desolvation efficiencies (see Fig. 1).

To test our hypothesis, we treated the acidified solution of gelatin with sodium tripolyphosphate ($Na_5P_3O_{10}$; TPP) to spatially entrap gelatin strands to form nanoclusters (see ES and Fig. S1a) [36]. Upon

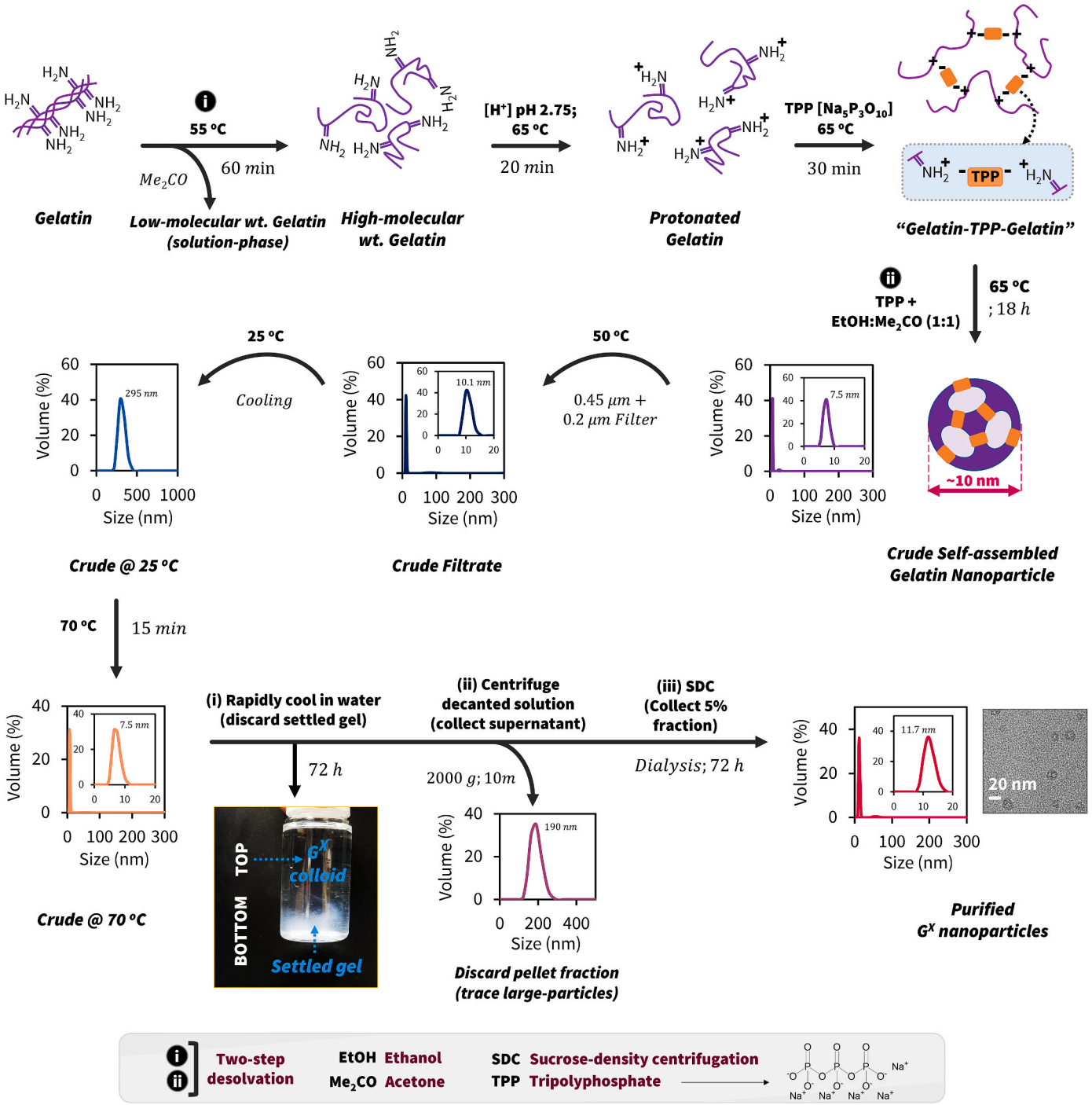

Fig. 1. Synthesis of G^X. Synthesis and purification of 10 nm gelatin nanoparticles (G^X) using TPP as a crosslinker followed by nanoprecipitation.

treatment of the nanoclusters with Ethanol-Acetone mixture (v/v; 1:1), ~5 nm toroid-like ring structures were formed within few minutes of the reaction as evidenced by HR-TEM images (Fig. 2a). After the completion of the reaction, the toroid structures self-assembled to form uniform 10 nm sized polyhedral structures (Figs. 2b and S2). We believe the intermediate toroid-like units may play a crucial role in the hierarchical self-assembly process to create the higher-order geometries [37,38]. To confirm that phosphates in TPP mediated the assembly process, we performed STEM-EDS spectra of the gelatin nanoparticle, and it showed the presence of phosphorus within the framework (Fig. S1b). We varied the gel-sol:Nanoprecipitant ratio (3:10 v/v) to control the rate of nanoprecipitation, and it resulted in the formation of a homogenous ~10 nm porous hollow structures (G^X) (Figs. 2b, 2c, and S2). The nanoparticle structure resembled a complex class II geodesic polyhedron with rotational vertexes, thickness around ~1.6 nm with a cavity around 5–10 nm (Fig. S2). The purified G^X showed a hydrodynamic diameter of 10 ± 3 nm with a +20 mV zeta potential (Fig. 2c and d, and **S3**). This process is the first reported facile synthesis of ultra-small protein-based nanoparticle structures in literature, to the best of our knowledge [20, 39–52].

3.2. 3D structure of G^X

We performed an in-depth image analysis to understand the 3D geometry of G^X to obtain insight into the self-assembly of these nanoparticles. We used HR-TEM images of G^X to map the local thickness and distance between the pixel intensities [53]. Further, using these resolved distance-maps, we created 3D surface plots at various angles (Fig. 3a). Specifically, we generated iterative volumetric models (Fig. 3b; *models i, ii, and iii*) and converted them to 3D surface plots that best represent G^X morphology (Fig. 3b) [54]. The structures were polyhedron in nature with rotational vertexes, as seen in the HR-TEM images (Figs. 2 and 3a, and **S2**). We predict that each higher-order G^X nanostructure consists of toroid-like building blocks based on the reconstructed volumetric models. The self-assembly process created a porous void in the structure of G^X. Indeed, the thin shell coupled with the hole inside the structure posed a significant challenge in recording HR-TEM of G^X (see ES) [55]. On the other hand, the size and density of G^X rendered themselves to scatter incident photons, enabling nanoparticles to be monitored by dynamic light scattering (DLS) technique [56].

3.3. Optimization of G^X synthesis

We asked the following questions with regards to the use of cross-linking agent, TPP: (*i*) Whether the TPP should be added before or after the desolvation step? and (*ii*) what is the optimum amount of TPP required to obtain uniform size G^X? To answer to the first question, we performed a series of reactions wherein we added TPP before or after the nanoprecipitation (or desolvation) step. As presented in the earlier sections, TPP bridges ammonium ions present in the backbone of gelatin strands. If the antisolvent precipitates gelatin, then the molecular arrangement will be disrupted and TPP would become incapable to form ionic bridges. As predicted, the addition of TPP after desolvation led to formation of non-homogenous nanoparticle populations with larger sizes (Figs. 4a and S4). As expected, addition of TPP before the precipitation step resulted in uniform size G^X formation (Fig. 4a). The study further confirms that TPP should be added before desolvation as it mediates the ionic bond to enable the self-assembly process and generate uniform size G^X (Fig. 4a). To answer the second question, we systematically increased the concentration of TPP (0; 0.1; 0.4; 1 or 2.5 mg/mL) in the nanoprecipitant solution and added it during the second desolvation step. The results showed that, up to a certain concentration (0.4 mg/mL) the reaction is resilient, and the size of the particle showed no variation (Fig. 4b). But, after the threshold concentration, the gelatin particles precipitated from the reaction. As we increased the TPP concentration, the amount of nanoprecipitant required to generate particles decreased proportionally. Based on our experiments, we found that ~200 μL of 0.5% TPP in the nanoprecipitant solution (0.1 mg/mL) was optimum to form uniform sized G^X (Fig. 4b).

Next, we studied the influence of desolvation mixture, ethanol: acetone, in the size of the G^X nanoparticles. We used the following ratios −1:1; 1:2; 1:4 or 1:10 ($EtOH:Me_2CO$; v/v) to precipitate the nanoparticles and recorded the size by DLS. Both 1:1 and 1:2 showed no variation in the final G^x formation, and the sizes were uniform. However, increasing the ratio of acetone to 1:4 or 1:10, resulted in turbidity of the solution indicating the aggregation of gelatin (Fig. 4c). These results agreed with previous literature which has shown denaturation led to increased particle size [35,57]. Based on the results, it is apparent

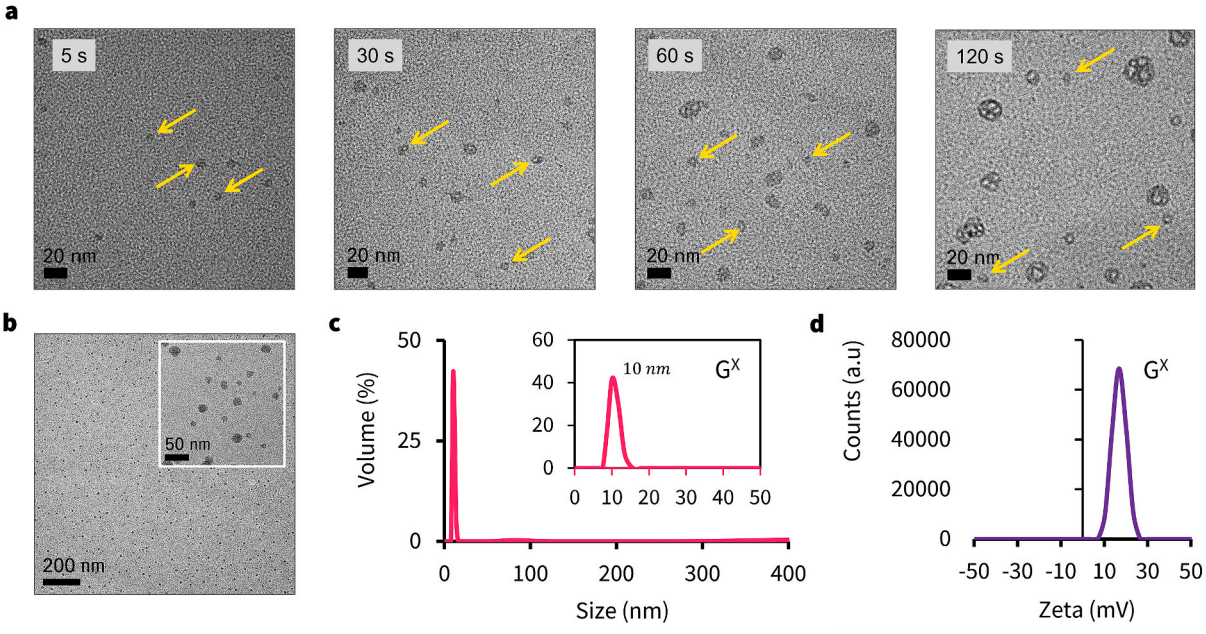

Fig. 2. Characterization of G^X. (a) HR-TEM images of the reaction mixture during the initial stages of the synthesis of G^X. The images show the formation of primordial toroid-like nanostructures (denoted by arrows), (b) HR-TEM images of purified G^X nanoparticles, (c) DLS, and (d) Zeta potential spectra for G^X.

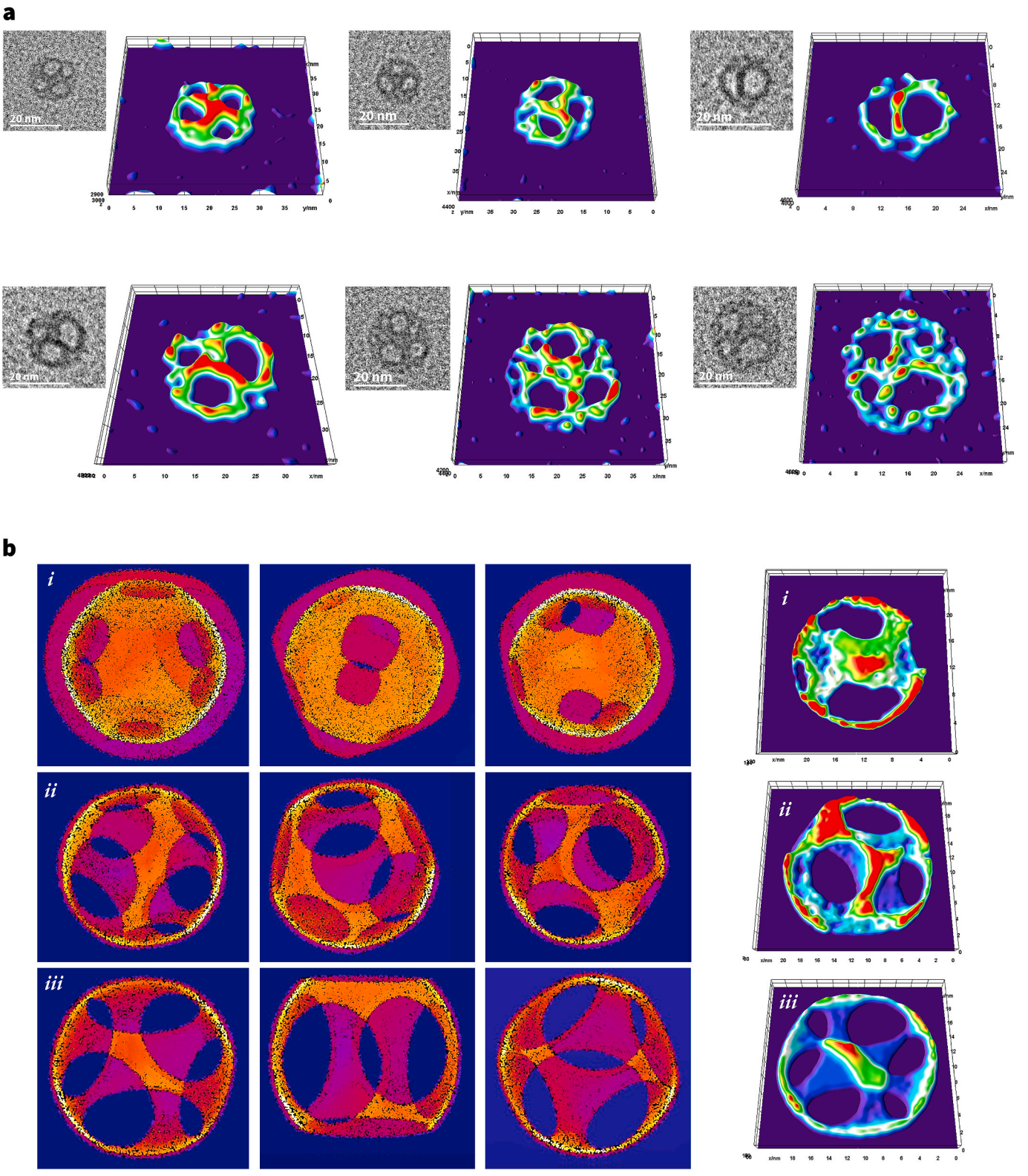

Fig. 3. Structure of G^X. (a) 3D surface plot of single G^X nanoparticles analyzed using distance mapped HR-TEM images, and (b) Approximated volumetric models with their representative 3D surface plot. Models ***i***, ***ii***, and ***iii*** represent higher-order polyhedral geometries.

that a 1:1 ethanol:acetone mixture was optimum in producing a homogenous colloidal solution without any visible precipitation (Fig. 4c).

The pH of the reaction determined the number of protonated amines in the backbone of gelatin. The pI of the gelatin type-A that we used in this study was between pH 7–9 [8,58]. Therefore, we chose to study the influence of pH (2, 2.75, and 5.6) in the size and homogeneity of generated G^X nanoparticles. If the pH of the solution was <6 (acidic) then the particles were smaller in size (Fig. S5a) [8,58]. Even though the smaller particles are formed at pH 5.6, (the native pH of gel-sol is 5.0 at 25 °C) the solution was glassy, and the precipitation ensued rapidly. The

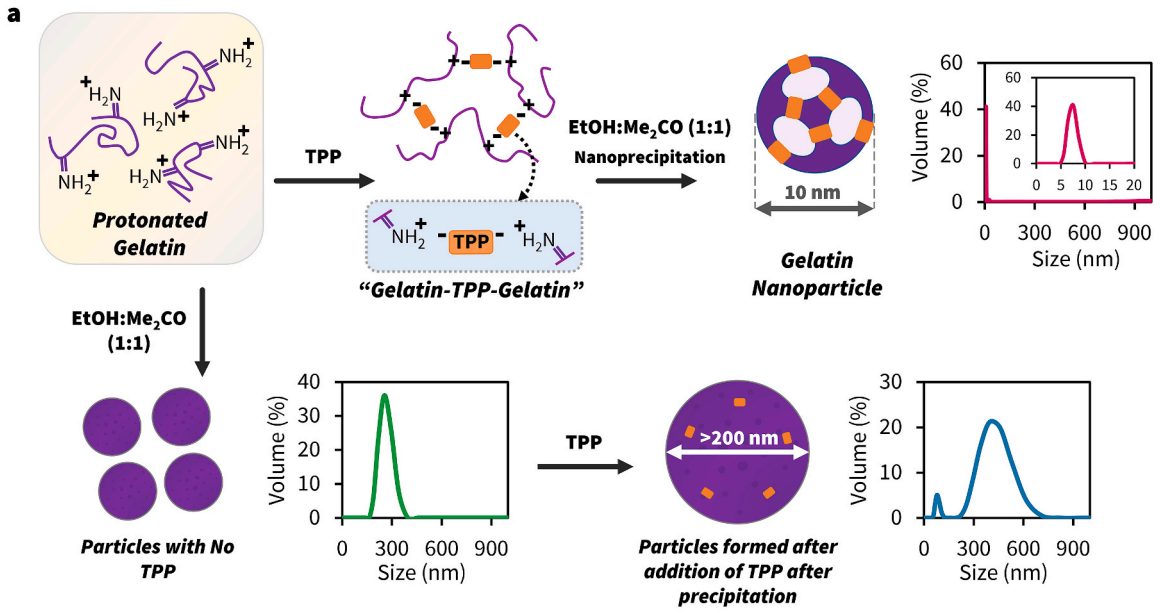

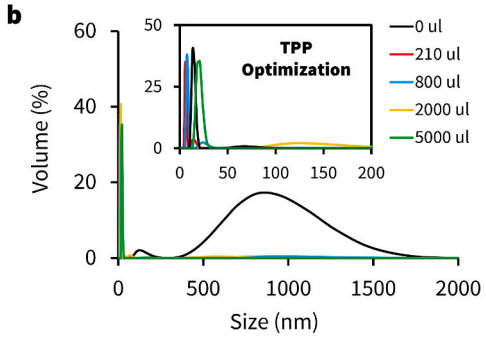

TPP (0.5%)	Hyd. Size (nm)	SE	PdI	Nanoprecipitant (ml)	Observation	Stability
0 µl	644.3	104.8	0.5	13.0	Whitish Opaque	Small ppt
210 µl	7.9	0.8	0.4	10.0	Whitish Opaque	Colloidal
800 µl	9.7	1.0	0.8	6.0	Whitish Translucent	Turbid
2000 µl	14.0	0.6	0.8	5.0	Glassy Translucent*	Small ppt
5000 µl	20.3	3.2	0.5	4.0	Glassy*	Large ppt

*Higher TPP reactions did not require reheating

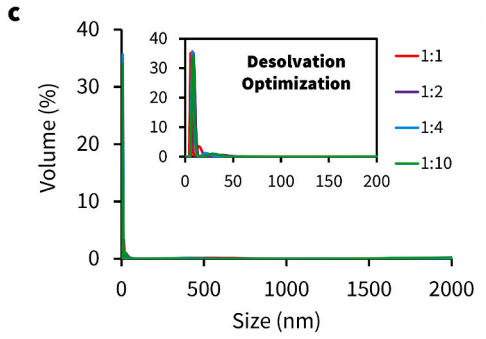

Ethanol: Acetone	Hyd. Size (nm)	SE	PdI	Nanoprecipitant (ml)	Observation	Stability
1:1	7.9	0.8	0.5	10.0	Whitish Opaque	Colloidal
1:2	7.5	0.4	0.7	9.0	Whitish Opaque	Colloidal
1:4	8.2	1.4	0.9	6.0	Whitish Opaque	Turbid
1:10	8.0	1.0	0.9	5.0	Whitish Opaque	Turbid

Fig. 4. Optimization of G^X synthesis. (a) Presence of TPP before the addition of nanoprecipitant promotes self-assembly of G^X nanoparticles, evident by DLS spectroscopy. (b) Optimization of TPP concentration in nanoprecipitant-mixture added to reaction solution for formation of G^X. (c) Optimization of Ethanol:Acetone ratio (nanoprecipitant-solution) added to reaction solution for formation of G^X.

precipitation may be due to lower repulsion between gelatin units [34]. On the other hand, lowering the pH $\leq$ 2 required more antisolvent to form nanoparticles, thereby changing the nanoprecipitant:gelatin ratios and causing visible destabilization. Based on our data, we found that pH 2.75 is optimum to form G^X (Fig. S5a). Also, we studied the effect of salt (10 mM NaCl) or sugar (10% sucrose) in gel sol in the formation of nanoparticles [5,59]. The results showed that formation of G^X was unhindered by either of the molecules further reiterating no influence on the ionic interactions between ammonium ions and TPP molecules (Fig. S5b). Finally, we attempted to synthesize G^X by controlling the reaction-temperature and varying the crosslinkers (Fig. S6). But these methods showed poor reproducibility.

3.4. *In vitro spheroid penetration by G^X nanoparticles*

The aim of this study was to evaluate the penetration characteristics of three different sized gelatin nanoparticles into 3D tumor spheroids. GNPs contain functional groups to either covalently or electrostatically bond dye molecules; in this study, we surface adsorbed Rhodamine-B (RhB) or covalently conjugated Cyanine-5 (Cy5) molecules to form G^M-dye (M = X (10 nm), L (50 nm), or CC (200 nm); dye = RhB or Cy5) constructs [8,29,32]. We characterized the conjugates using TEM, DLS, zeta, and fluorescence spectroscopy (Fig. 5). In parallel, we developed both ovarian and non-small cell lung cancer (NSCLC) spheroids based on the manufacturer's protocols (see ES). The spheroid formation was monitored by bright-field microscopy. After 5 days, the spheroids were

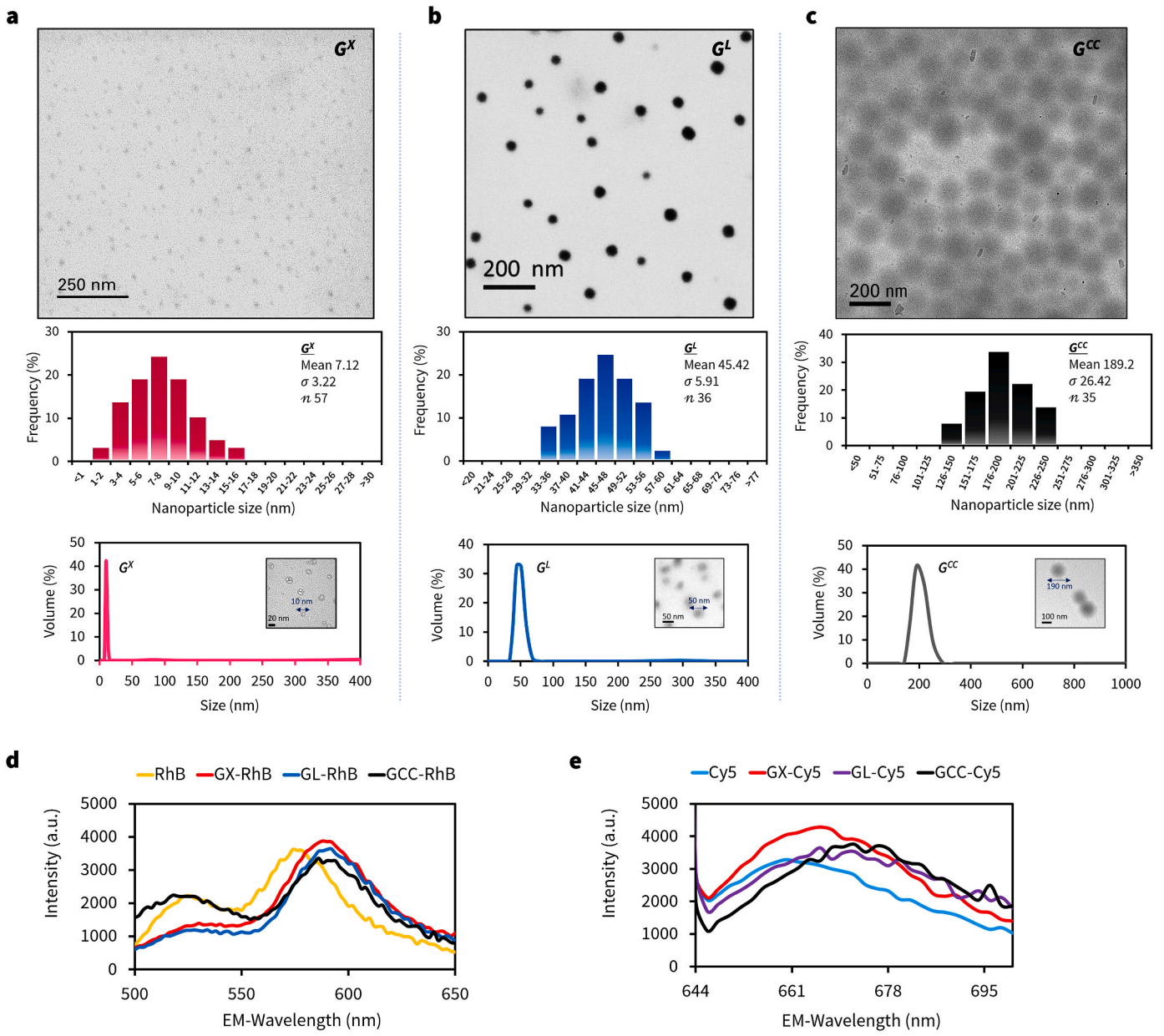

Fig. 5. Characterization of G^X, G^L, G^{CC} and respective dye-tagged constructs. STEM image, corresponding size-distribution histogram and DLS spectra with TEM-inset for (a) 10 nm G^X, (b) 50 nm G^L and (c) 200 nm G^{CC} nanoparticles. Fluorescence spectra of dye-tagged (Rhodamine-B or Cyanine-5) G^X, G^L or G^{CC} nanoparticles for the treatment with 3D tumor spheroids.

formed, and the sizes of 197 ± 15 μm (NCI-ADR-RES), and 173 ± 12 μm (A549) were selected for the study. The cells were tightly packed in ovarian cancer (NCI-ADR-RES) spheroids compared with that of NSCLC (A549).

Confocal fluorescence microscopy (CFM) can be used as a tool to evaluate the penetration of the fluorescent G^M-dye constructs in tumor spheroids. As a first step, we incubated the spheroids with different concentrations of free dye or constructs to determine the treatment concentration for the imaging study. The chosen concentrations of the G^M-dye (equated by fluorescence intensity) did not show any toxicity in cells and the spheroid integrity was maintained (Fig. S7). After selecting the working concentration, the ovarian and NSCLC spheroids were incubated with G^M-dye for a period of 6 h. The spheroids were imaged at different depths using CFM (Figs. 6, and 7), and linear Z compensation was applied to account for the variable z-depth reduction in signal resulting from the slight variation in compactness between spheroids.

To provide a preliminary qualitative picture of the CFM data, we segmented the spheroid into three sections: outer (10–20 μm); inner (30–40 μm); and deep (50 μm). In the case of RhB loaded particles, the G^{CC}-RhB particles were brightly seen in the outer region and faintly in the inner region of the spheroid, however, no fluorescence was observed in the deep region of both NCI-ADR-RES and A549 spheroids (Fig. 6). On the other hand, the G^L-RhB and G^X-RhB particles were observed in all regions of the spheroid. Based on this preliminary analysis, we suspect that the order of penetrance into the deep tumor region is: G^X-RhB = G^L-RhB » G^{CC}-RhB. In the case of Cy5 loaded particles, G^X-Cy5 particles were more prominent in all regions of the spheroid compared to G^L-Cy5 or G^{CC}-Cy5. Based on this preliminary analysis, we suspect that the order of penetrance into the deep tumor region is: G^X-Cy5>G^L-RhB = G^{CC}-RhB.

The linear Z compensation applied during imaging precludes the comparison of raw intensity between sections/spheroids. Therefore, to enable the comparison, the relative mean intensity of the inner and outer regions of each section was calculated (inner defined as 2/3rd of the

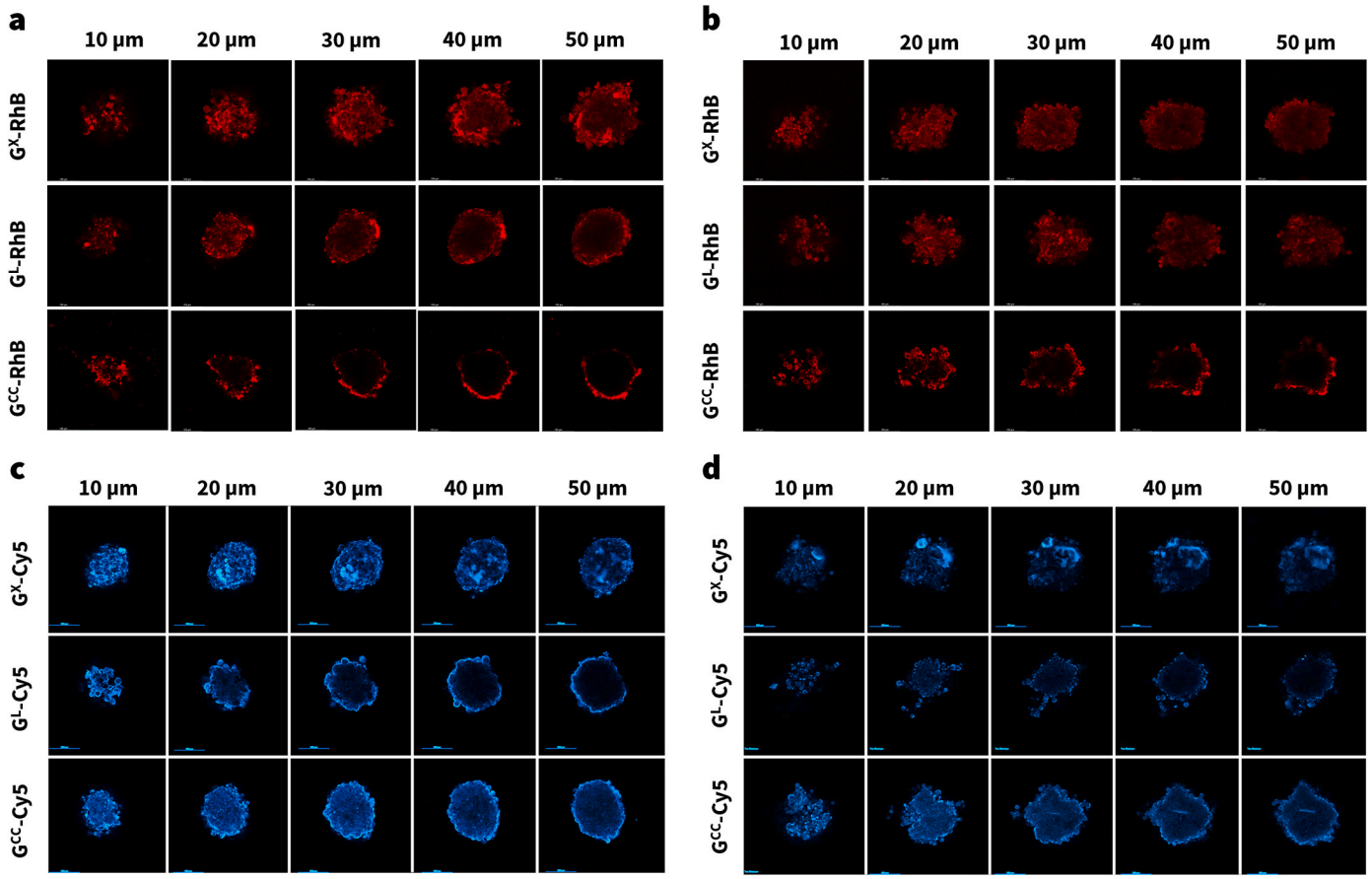

Fig. 6. 3D Spheroids treated with G^M-Dye constructs. Confocal Fluorescence Microscopy (CFM) images of 3D tumor spheroids treated with G^X, G^L or G^{CC} nanoparticles tagged with Rhodamine-B (RhB), or Cyanine-5 (Cy5) dye, at various penetration depths (10–50 μm). (a and b respectively) NCI-ADR-RES and A549 spheroids treated with G^M-RhB constructs. (b and c respectively) NCI-ADR-RES and A549 spheroids treated with G^M-Cy5 constructs. The images are representative. The difference in linear z compensation applied during imaging prevented comparisons of raw-intensity between sections/spheroids. (M = X, L or CC).

radius of each section; Fig. 7a and **b**). The average relative mean intensity values ($n \leq 3$) hinted that G^X and G^L show greater penetration when compared to G^{CC}, except in the case of Cy5 constructs where G^{CC} suggested slightly better penetration than G^L. The data ($n \leq 3$) also suggested that G^X showed greater penetration than G^L in the case of NCI-ADR-RES (RhB and Cy5) and A549 (Cy5 only). G^X-RhB and G^L-RhB were similar when the data point spread was compared, making it difficult to conclusively claim that G^X showed greater penetration that G^L (Fig. 7c and d).

Next, we treated the spheroids for 14 h with the constructs and z-stacked the CFM images to view its 3D reconstruction (rotated along x-axis); the 3D volume suggested higher G^X-RhB penetration within both NCI-ADR-RES or A549 tumor spheroids than G^L-RhB or G^{CC}-RhB constructs (Supplementary video - Sv). It is important to note that, 200 nm G^{CC}-dye constructs formed a shell around the outer layer of the tumor spheroids indicating high tumor-surface localization (Fig. 6 and Supplementary video - Sv). This observation was in line with the previous literature studies, wherein larger particles are known to exhibit poor permeation within tumors [18]. Pratiwi and coworkers evaluated the tumor penetration of mesoporous silica nanoparticles with sizes 25, 50, and 200 nm using two-photon excitation microscopy (TPEF) [15]. Among the nine different parameters compared, they found both the shape and size of the particles were crucial in determining the penetration characteristics. The study showed that 25 nm particles had better penetration than the 50 nm; however, the 200 nm particles mainly resided on the surface. In another study using polymeric micelles of sizes 30, 50, 70, and 100 nm, Cabral and coworkers showed that 30 nm particles had better deep tumor penetration capability than others [17].

Previous studies have shown that smaller-sized particles are more efficient in passing through intercellular space with effective spatial distribution within the tumor spheroids [13,15,60,61]. Even in our studies, G^X nanoparticles showed better penetration than G^{CC}. Other factors such as charge, shape, treatment duration, or how the dye is bonded with the nanoparticles could also play a role in tumor penetrability. Therefore, further investigation is warranted to comprehensively study the effect of these factors on deep tumor penetration of G^X [18,61,62].

3.5. Encapsulation of drug or contrast agents in G^X

Next, we examined the ability of G^X to encapsulate different materials. Indeed, the TEM images and 3D volume reconstruction models predicted that the structure of G^X contains a void inside.

The G^X structure prompted us to evaluate whether it can encapsulate the drug or imaging agent inside the void. Further, gelatin is ampholytic, which means that the backbone can attach to both hydrophobic and hydrophilic molecules [2,63]. We chose two drugs for encapsulation, doxorubicin (DOX) and cisplatin (CP), to generate (G^X(R); R = DOX or CP) (Fig. 8a). We mixed predetermined concentrations of the drug with protonated gelatin (Drug: Gelatin ~3.8% w/w) and followed the same steps used for synthesizing G^X. After the synthesis, we centrifuged the reaction mixture and washed the precipitate to remove free drug. The hydrodynamic sizes of the final product were ~12–20 nm with PDI of ~0.5–0.8. The cisplatin encapsulated G^X was slightly larger (~19 nm) (Fig. S8). The zeta potential of G^X(R) was positive and greater than 20 mV. The TEM images of the G^X(R) are shown in Fig. 8b. The G^X(R) particles were darker in TEM images than pristine G^X; especially, the

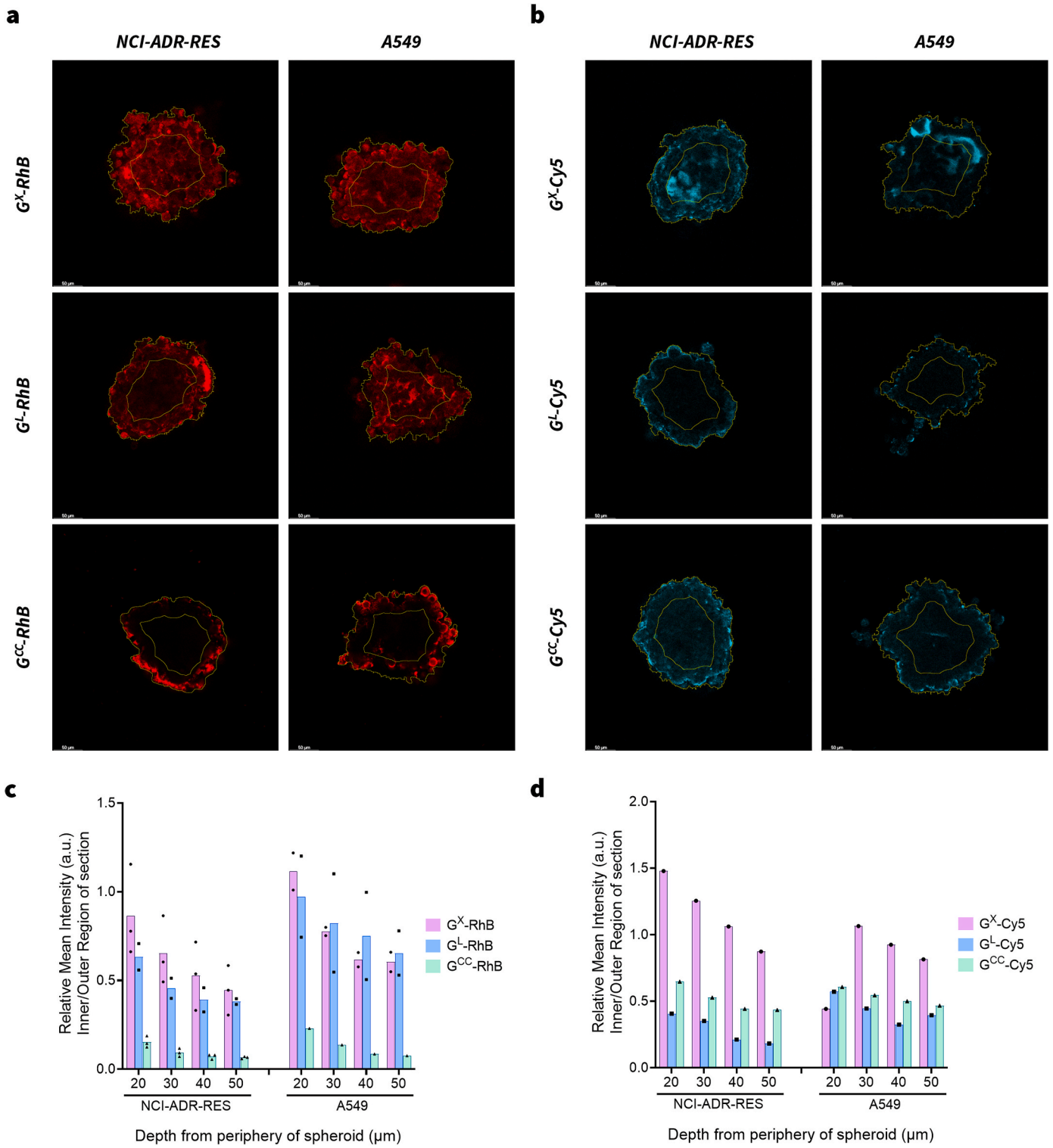

Fig. 7. Spheroid segmentation analysis to evaluate the penetration of G^M-Dye constructs. Representative spheroid sections (30 μm depth from periphery of spheroid) from spheroids ($n \leq 3$) treated with G^X, G^L or G^{CC} nanoparticles tagged with Rhodamine-B (RhB) or Cyanine-5 (Cy5) dye. (a) NCI-ADR-RES and A549 spheroids treated with G^M-RhB constructs. (b) NCI-ADR-RES and A549 spheroids treated with G^M-Cy5 constructs. Relative mean-intensity values of inner section vs periphery at various penetration depths for each group treated with (c) G^M-RhB constructs or (d) G^M-Cy5 constructs. (M = X, L or CC).

cisplatin loaded G^X absorbed electrons effectively and it appeared significantly darker. We recorded the UV–Visible absorption/-fluorescence spectra of G^X (DOX), and it showed a characteristic absorbance at 490 and emission at 590 nm (Fig. 8c). Further, the STEM-EDS spectra of G^X (CP) showed platinum peaks confirming the presence of drug trapped inside (Fig. 8d). The study showed that the void in G^X is ideally suited to encapsulate drugs and still retain their size. Importantly, this data establishes the potential of G^X to serve as delivery agents.

We also evaluated the potential of G^X to encapsulate computed tomography (CT) imaging contrast agents such as Iodixanol (IO) within its porous structure. Previous studies have encapsulated X-ray contrast

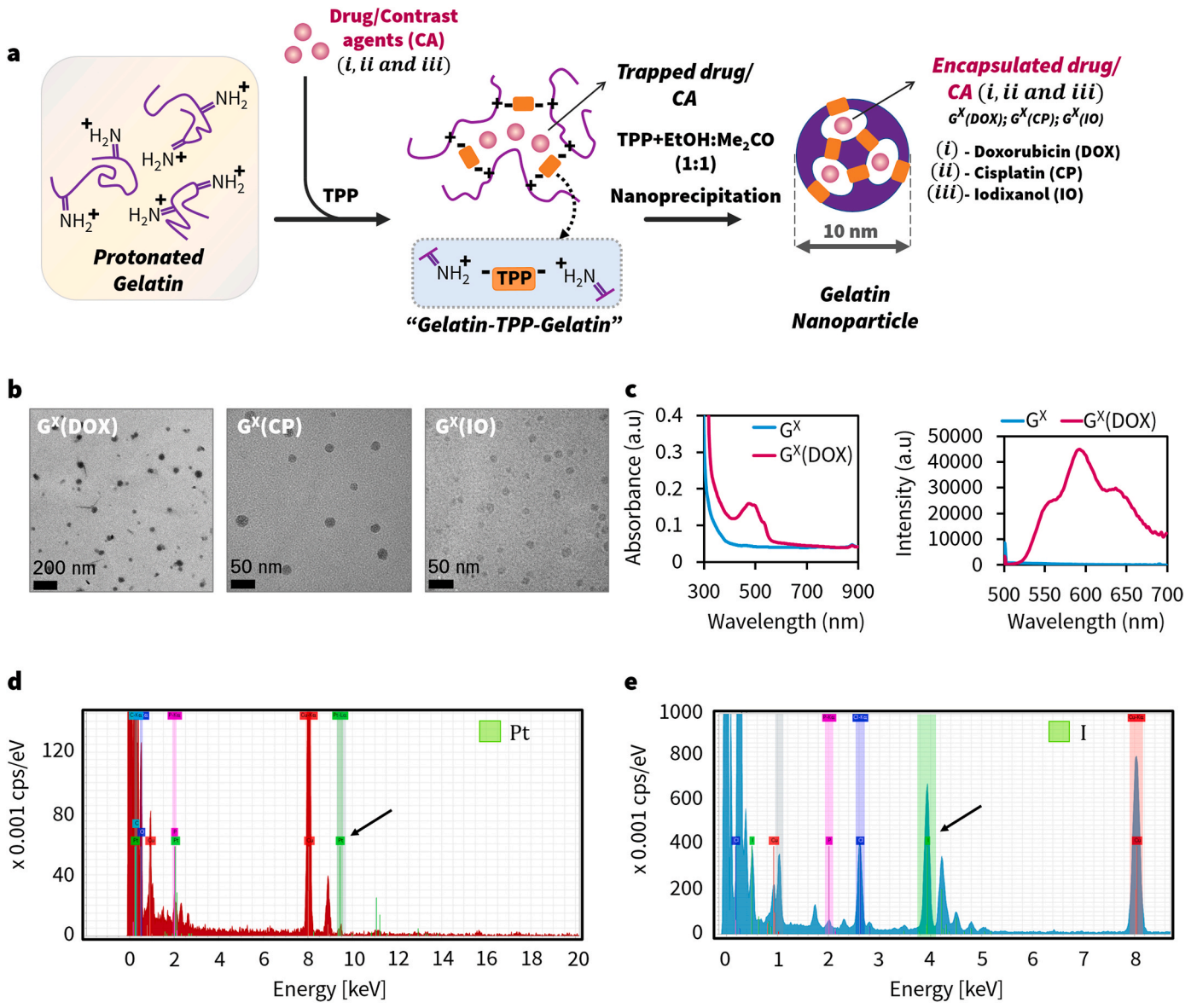

Fig. 8. Synthesis and characterization of G^X (Drug) or G^X (Contrast-agent) constructs. (a) Synthesis of drug/contrast-agent encapsulated G^X nanoparticles (b) TEM images of G^X (DOX), G^X (CP) and G^X (IO); images show the morphology of the particles is retained. (c) Absorbance and fluorescence spectra of G^X (DOX) and STEM-EDS spectra for (d) Platinum peak in G^X (CP) and (d) Iodine peak in G^X (IO).

agents within liposomes or polymeric nanoparticles for diagnostic applications [64,65]. As G^X possess a similar framework, we hypothesized that the nanoparticles can encapsulate IO within the matrix. In our study, we mixed IO with gelatin sol (IO:Gelatin ~7.4% w/w) and nanoprecipitated to form G^X (IO) (Fig. 8a). As shown in Fig. 8b, HR-TEM images confirm the morphology of the G^X was preserved. The size of HR-TEM agreed with DLS data (~8 nm) showing negligible differences to its hydrodynamic size (Fig. S8). Notably, a slight increase in zeta potential of ~25 mV was observed (Fig. S8). We characterized G^X (IO) using EDS to detect presence of iodine (I) in the construct and identified a specific peak corresponding to I, indicating presence of IO within the construct (Fig. 8e). Taken together, the data shows that G^X nanoparticles can encapsulate both drugs or contrast agents during the self-assembly process and have a potential to serve as ideal theranostic agents.

3.6. *Encapsulation or surface attachment of gold nanoparticles with G^X*

Next, owing to the unique size and morphology of G^X, we explored its use as a building block to synthesize hybrid nanostructures. A variety of hybrid nanostructures with multidimensional components have been shown to provide enhanced therapeutic or diagnostic benefits [66,67]. Specifically, when using a single sized-nanoparticle there may be inherent limitations to pharmacokinetics, tumor localization and intra-tumor spatial distribution [18,62]. For example, larger particles (>60 nm) localize in the tumor vasculature and target tumor surface efficiently but exhibit low penetration; whereas, smaller particles (<60 nm) penetrate deeply and spatially distribute within the tumor but localize poorly. By combining two different sizes or functionalities, these limitations can be further mitigated. Particularly, the "*tanker*" and "*barge*" motifs that form the basis of the two hybrid nanocomposite design strategies, can be used to form dual-nanoparticle hybrids [66]. In this approach, smaller particles are encapsulated within a larger hollow particle. In this study, we developed the following hybrid nanomaterials by entrapping ultra-small gold nanoparticles (AuNP) within the cavity of G^X (Fig. 9a). For forming dual-nanoparticle G^X (Au) hybrid, AuNP was mixed with gel sol and then nanoprecipitated. As seen in HR-TEM images, 2 nm AuNP were effectively entrapped within the structure of G^X (~10 AuNP/G^X) (Fig. 9b and Fig. S9). DLS spectra showed minimal

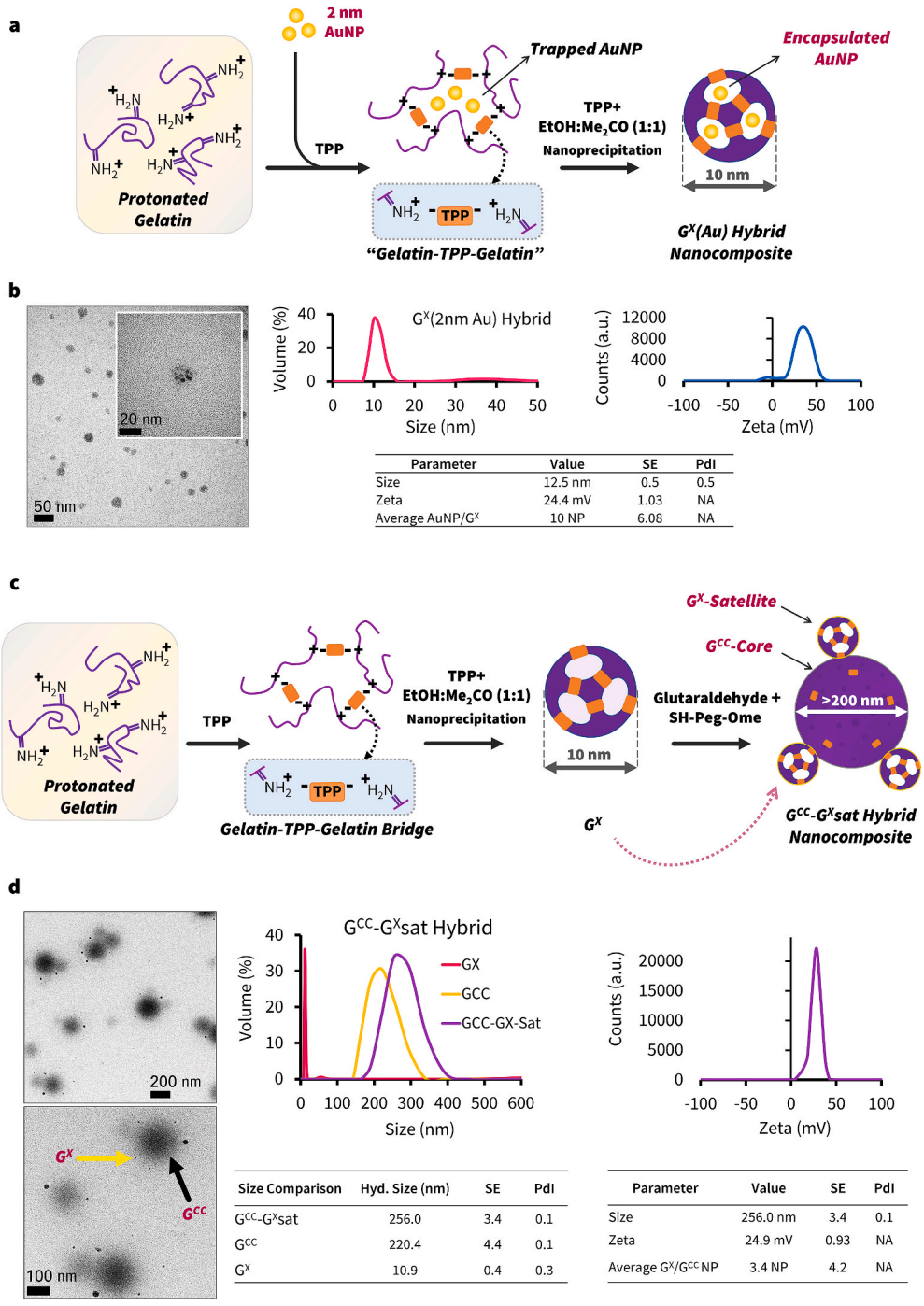

Fig. 9. G^X Hybrid Nanostructures. (a) Synthesis of gold nanoparticle-encapsulated G^X hybrid nanocomposites, (b) HR-TEM images, DLS and Zeta potential spectra and data for G^X (2 nm AuNP) hybrid. (c) *In-situ* formation of G^{CC}-G^X core-satellite nanocomposites, and (d) HR-TEM images, DLS, and Zeta potential spectra for G^{CC}-G^Xsat hybrid nanoparticles. (For interpretation of the references to color in this figure legend, the reader is referred to the Web version of this article.)

change to the hydrodynamic size as the AuNP was encapsulated. The entrapment efficiency varied based on the surface coating on the AuNP (Fig. S10a). By changing the surface characteristics or size of AuNP, we observed AuNP would attach to the surface of G^X as seen in HR-TEM images and a correlated shift in their DLS spectra (Fig. S10a). Such hybrid assemblies can be used to deliver nanoparticles deep within the tumor. Potentially, such assemblies could be functionalized, where each nanocomponent would carry a contrast agent or drug for effective theranostics [68,69].

3.7. *Multi-sized nanoparticles in single nanostructure using G^X*

For developing core-satellite hybrids using gelatin matrix, we developed a novel *in situ* synthesis wherein G^X and G^{CC} particles were synthesized in the same reaction solution with a mixture of crosslinking agents (Fig. 9c). In this reaction, G^X was first synthesized followed by addition of a mixture containing both TPP and glutaraldehyde (GLU). GLU is known to crosslink the lysine ε-amino groups and N-terminal amino acids of the gelatin chain [70] and has been used in numerous studies for forming larger 200 nm G^{CC} [6,8,32,58,71,72]. As shown in Fig. 9d, HR-TEM images show the formation of G^{CC}-G^Xsat core-satellite

assemblies where 150–200 nm GNPs were decorated with an average of ~4 G^X particles (Fig. 9d). Prior attempts to form such core-satellite assemblies often involved metal-metal or metal-organic frameworks based on electrostatic or covalent linking methods [73–77]. Similarly, in a previous study we have developed core-satellite assemblies of gelatin nanoparticles and AuNP using microfluidic synthesis [33]. Notably, the difference in this synthesis was that G^{CC} was formed in a G^X reaction solution and G^X was not separately attached. As such these multi-dimensional hybrids were self-assembled *in situ* and each nanocomponent (200 nm and 10 nm) may be used for efficient tumor localization and deep penetration [19,22]. We also found that by changing the amount of glutaraldehyde in the reaction we could tune the size of the satellite nanoparticles (Fig. S10b). These results demonstrate that dual-nanoparticle based hybrid nanostructures can be used for increasing the tumor penetration efficiency and other applications where size-based multi-staged delivery may be appropriate. Altogether, G^X nanoparticles present a new class of porous spherical ultra-small protein-based nanoparticles that can be used towards development of nanomedicine and diagnostics. Future studies to understand the mechanism of assembly kinetics may be beneficial towards exploring these potential applications.

4. Conclusion

This study has established a reproducible facile route to synthesize ultra-small 10 nm protein-based Gelatin nanoparticles (G^X) and explored its physical properties. G^X had a characteristic polyhedral porous structure with positive zeta potential and contained functional groups on the surface. To study the deep tumor penetration capabilities of smaller-sized G^X, we compared the penetration efficiency of nanoparticles of three different sizes: 10 nm G^X, 50 nm G^L and 200 nm G^{CC}. In general, the smaller-sized GNPs showed better spheroid penetration compared to the larger nanoparticles. Furthermore, we developed strategies to encapsulate drugs or contrast agents within G^X. These agents can be used for delivering precision medicine or diagnosing diseases. We also developed multifunctional hybrid nanostructures using G^X, wherein 2 nm gold nanoparticles were encapsulated within G^X, or formed G^{CC}-G^X core-satellite hybrid nanocomposites. We anticipate these hybrid nanocomposites have outstanding potential for developing a new class of multi-staged payload delivery vehicles. In summary, this study generated a novel functional platform based on 10 nm biodegradable protein-based nanoparticles for advanced biomedical applications.

Declaration of competing interests

The authors declare no competing financial interests.

CRediT authorship contribution statement

Dhananjay Suresh: Conceptualization, Investigation, Writing – review & editing. **Agasthya Suresh:** Investigation, Writing – review & editing. **Raghuraman Kannan:** Investigation, Writing – review & editing.

Acknowledgement

The funding for the tumor spheroid studies were provided by the School of Medicine's Translational Research Informing Useful and Meaningful Precision Health (TRIUMPH) grant. We also thank Michael J and Sharon R Bukstein Endowment funds for supporting the design and development of novel nanoconstructs presented in this study.

Appendix A. Supplementary data

Supplementary data to this article can be found online at https://doi.org/10.1016/j.bioactmat.2022.02.035.

References

[1] M. Diba, G.L. Koons, M.L. Bedell, A.G. Mikos, 3D printed colloidal biomaterials based on photo-reactive gelatin nanoparticles, Biomaterials (2021) 274, https://doi.org/10.1016/j.biomaterials.2021.120871.

[2] A.O. Elzoghby, Gelatin-based nanoparticles as drug and gene delivery systems: reviewing three decades of research, J. Contr. Release 172 (2013) 1075–1091, https://doi.org/10.1016/j.jconrel.2013.09.019.

[3] D. Li, K. Chen, H. Tang, S. Hu, L. Xin, X. Jing, Q. He, S. Wang, J. Song, L. Mei, R. D. Cannon, P. Ji, H. Wang, T. Chen, A logic-based diagnostic and therapeutic hydrogel with multi-stimuli responsiveness to orchestrate diabetic bone regeneration, Adv. Mater. (2021), https://doi.org/10.1002/adma.202108430.

[4] Z. Mu, K. Chen, S. Yuan, Y. Li, Y. Huang, C. Wang, Y. Zhang, W. Liu, W. Luo, P. Liang, X. Li, J. Song, P. Ji, F. Cheng, H. Wang, T. Chen, Gelatin nanoparticle-injectable platelet-rich fibrin double network hydrogels with local adaptability and bioactivity for enhanced osteogenesis, Advanced Healthcare Materials 9 (2020), https://doi.org/10.1002/adhm.201901469.

[5] P. Khramtsov, O. Burdina, S. Lazarev, A. Novokshonova, M. Bochkova, V. Timganova, D. Kiselkov, A. Minin, S. Zamorina, M. Rayev, Modified desolvation method enables simple one-step synthesis of gelatin nanoparticles from different gelatin types with any bloom values, Pharmaceutics 13 (2021), https://doi.org/10.3390/pharmaceutics13101537.

[6] S. Amjadi, H. Hamishehkar, M. Ghorbani, A novel smart PEGylated gelatin nanoparticle for co-delivery of doxorubicin and betanin: a strategy for enhancing the therapeutic efficacy of chemotherapy, Mater. Sci. Eng. C 97 (2019) 833–841, https://doi.org/10.1016/j.msec.2018.12.104.

[7] Z. Lu, T.-K. Yeh, J. Wang, L. Chen, G. Lyness, Y. Xin, M.G. Wientjes, V. Bergdall, G. Couto, F. Alvarez-Berger, C.E. Kosarek, J.L.S. Au, Paclitaxel gelatin nanoparticles for intravesical bladder cancer therapy, J. Urol. 185 (2011) 1478–1483, https://doi.org/10.1016/j.juro.2010.11.091.

[8] D. Suresh, A. Zambre, S. Mukherjee, S. Ghoshdastidar, Y. Jiang, T. Joshi, A. Upendran, R. Kannan, Silencing AXL by covalent siRNA-gelatin-antibody nanoconjugate inactivates mTOR/EMT pathway and stimulates p53 for TKI sensitization in NSCLC, Nanomed. Nanotechnol. Biol. Med. (2019) 20, https://doi.org/10.1016/j.nano.2019.04.010.

[9] B. Khodashenas, M. Ardjmand, A.S. Rad, M.R. Esfahani, Gelatin-coated gold nanoparticles as an effective pH-sensitive methotrexate drug delivery system for breast cancer treatment, Materials Today Chemistry 20 (2021), https://doi.org/10.1016/j.mtchem.2021.100474.

[10] D. Lee, S.-y. Jang, S. Kwon, Y. Lee, E. Park, H. Koo, Optimized combination of photodynamic therapy and chemotherapy using gelatin nanoparticles containing tirapazamine and pheophorbide a, ACS Appl. Mater. Interfaces 13 (2021) 10812–10821, https://doi.org/10.1021/acsami.1c02316.

[11] H. Wang, O.C. Boerman, K. Sariibrahimoglu, Y. Li, J.A. Jansen, S.C. G. Leeuwenburgh, Comparison of micro- vs. nanostructured colloidal gelatin gels for sustained delivery of osteogenic proteins: bone morphogenetic protein-2 and alkaline phosphatase, Biomaterials 33 (2012) 8695–8703, https://doi.org/10.1016/j.biomaterials.2012.08.024.

[12] H. Wang, Q. Zou, O.C. Boerman, A.W.G. Nijhuis, J.A. Jansen, Y. Li, S.C. G. Leeuwenburgh, Combined delivery of BMP-2 and bFGF from nanostructured colloidal gelatin gels and its effect on bone regeneration in vivo, J. Contr. Release 166 (2013) 172–181, https://doi.org/10.1016/j.jconrel.2012.12.015.

[13] A. Tchoryk, V. Taresco, R.H. Argent, M. Ashford, P.R. Gellert, S. Stolnik, A. Grabowska, M.C. Garnett, Penetration and uptake of nanoparticles in 3D tumor spheroids, Bioconjugate Chem. 30 (2019) 1371–1384, https://doi.org/10.1021/acs.bioconjchem.9b00136.

[14] E.C. Dreaden, L.A. Austin, M.A. Mackey, M.A. El-Sayed, Size matters: gold nanoparticles in targeted cancer drug delivery, Ther. Deliv. 3 (2012) 457–478, https://doi.org/10.4155/tde.12.21.

[15] F.W. Pratiwi, C.C. Peng, S.H. Wu, C.W. Kuo, C.Y. Mou, Y.C. Tung, P. Chen, Evaluation of nanoparticle penetration in the tumor spheroid using two-photon microscopy, Biomedicines 9 (2020), https://doi.org/10.3390/biomedicines9010010.

[16] L. Tang, N.P. Gabrielson, F.M. Uckun, T.M. Fan, J. Cheng, Size-dependent tumor penetration and in vivo efficacy of monodisperse drug–silica nanoconjugates, Mol. Pharm. 10 (2013) 883–892, https://doi.org/10.1021/mp300684a.

[17] H. Cabral, Y. Matsumoto, K. Mizuno, Q. Chen, M. Murakami, M. Kimura, Y. Terada, M.R. Kano, K. Miyazono, M. Uesaka, N. Nishiyama, K. Kataoka, Accumulation of sub-100 nm polymeric micelles in poorly permeable tumours depends on size, Nat. Nanotechnol. 6 (2011) 815–823, https://doi.org/10.1038/nnano.2011.166.

[18] W. Yu, R. Liu, Y. Zhou, H. Gao, Size-tunable strategies for a tumor targeted drug delivery system, ACS Cent. Sci. 6 (2020) 100–116, https://doi.org/10.1021/acscentsci.9b01139.

[19] X. Cheng, H. Li, X. Ge, L. Chen, Y. Liu, W. Mao, B. Zhao, W.-E. Yuan, Tumor-microenvironment- responsive size-shrinkable drug-delivery nanosystems for deepened penetration into tumors, Frontiers in Molecular Biosciences 7 (2020), https://doi.org/10.3389/fmolb.2020.576420.

[20] A. Kimura, J.-i. Jo, F. Yoshida, Z. Hong, Y. Tabata, A. Sumiyoshi, M. Taguchi, I. Aoki, Ultra-small size gelatin nanogel as a blood brain barrier impermeable contrast agent for magnetic resonance imaging, Acta Biomater. 125 (2021) 290–299, https://doi.org/10.1016/j.actbio.2021.02.016.

[21] S. Huo, H. Ma, K. Huang, J. Liu, T. Wei, S. Jin, J. Zhang, S. He, X.-J. Liang, Superior penetration and retention behavior of 50 nm gold nanoparticles in tumors, Cancer Res. 73 (2013) 319–330, https://doi.org/10.1158/0008-5472.Can-12-2071.

[22] C. Wong, T. Stylianopoulos, J. Cui, J. Martin, V.P. Chauhan, W. Jiang, Z. Popovic, R.K. Jain, M.G. Bawendi, D. Fukumura, Multistage nanoparticle delivery system for

deep penetration into tumor tissue, Proc. Natl. Acad. Sci. Unit. States Am. 108 (2011) 2426–2431, https://doi.org/10.1073/pnas.1018382108.
[23] S. Ruan, X. Cao, X. Cun, G. Hu, Y. Zhou, Y. Zhang, L. Lu, Q. He, H. Gao, Matrix metalloproteinase-sensitive size-shrinkable nanoparticles for deep tumor penetration and pH triggered doxorubicin release, Biomaterials 60 (2015) 100–110, https://doi.org/10.1016/j.biomaterials.2015.05.006.
[24] C.J. Coester, K. Langer, H. Von Briesen, J. Kreuter, Gelatin nanoparticles by two step desolvation a new preparation method, surface modifications and cell uptake, J. Microencapsul. 17 (2008) 187–193, https://doi.org/10.1080/026520400288427.
[25] A.T. Stevenson, D.J. Jankus, M.A. Tarshis, A.R. Whittington, The correlation between gelatin macroscale differences and nanoparticle properties: providing insight into biopolymer variability, Nanoscale 10 (2018) 10094–10108, https://doi.org/10.1039/c8nr00970h.
[26] L. Vaghi, M. Monti, M. Marelli, E. Motto, A. Papagni, L. Cipolla, Photoinduced porcine gelatin cross-linking by homobi- and homotrifunctional tetrazoles, Gels 7 (2021), https://doi.org/10.3390/gels7030124.
[27] A. Singh, J. Xu, G. Mattheolabakis, M. Amiji, EGFR-targeted gelatin nanoparticles for systemic administration of gemcitabine in an orthotopic pancreatic cancer model, Nanomed. Nanotechnol. Biol. Med. 12 (2016) 589–600, https://doi.org/10.1016/j.nano.2015.11.010.
[28] Y. Gwon, W. Kim, S. Park, S. Hong, J. Kim, A freezing and thawing method for fabrication of small gelatin nanoparticles with stable size distributions for biomedical applications, Tissue Engineering and Regenerative Medicine (2021), https://doi.org/10.1007/s13770-021-00380-x.
[29] D. Suresh, B. Jenkins, A. Zambre, A. Upendran, R. Kannan, Systematic evaluation of protein-based nanoparticles for stable delivery of small interfering RNA, J. Biomed. Nanotechnol. 16 (2020) 1169–1181, https://doi.org/10.1166/jbn.2020.2953.
[30] J. Schindelin, I. Arganda-Carreras, E. Frise, V. Kaynig, M. Longair, T. Pietzsch, S. Preibisch, C. Rueden, S. Saalfeld, B. Schmid, J.-Y. Tinevez, D.J. White, V. Hartenstein, K. Eliceiri, P. Tomancak, A. Cardona, Fiji: an open-source platform for biological-image analysis, Nat. Methods 9 (2012) 676–682, https://doi.org/10.1038/nmeth.2019.
[31] D. Lacalle, H.A. Castro-Abril, T. Randelovic, C. Domínguez, J. Heras, E. Mata, G. Mata, Y. Méndez, V. Pascual, I. Ochoa, SpheroidJ: an open-source set of tools for spheroid segmentation, Comput. Methods Progr. Biomed. 200 (2021), https://doi.org/10.1016/j.cmpb.2020.105837.
[32] R. Srikar, D. Suresh, A. Zambre, K. Taylor, S. Chapman, M. Leevy, A. Upendran, R. Kannan, Targeted nanoconjugate co-delivering siRNA and tyrosine kinase inhibitor to KRAS mutant NSCLC dissociates GAB1-SHP2 post oncogene knockdown, Sci. Rep. 6 (2016), https://doi.org/10.1038/srep30245.
[33] R. Srikar, D. Suresh, S. Saranathan, A. Zambre, R. Kannan, Three-dimensional nanocomposites: fluidics driven assembly of metal nanoparticles on protein nanostructures and their cell-line-dependent intracellular trafficking pattern, Langmuir 32 (2016) 4877–4885, https://doi.org/10.1021/acs.langmuir.6b00911.
[34] S.M. Ahsan, C.M. Rao, The role of surface charge in the desolvation process of gelatin: implications in nanoparticle synthesis and modulation of drug release, Int. J. Nanomed. 12 (2017) 795–808, https://doi.org/10.2147/ijn.S124938.
[35] S. Azarmi, Y. Huang, H. Chen, S. McQuarrie, D. Abrams, W. Roa, W.H. Finlay, G. G. Miller, R. Löbenberg, Optimization of a two-step desolvation method for preparing gelatin nanoparticles and cell uptake studies in 143B osteosarcoma cancer cells, J. Pharm. Pharmaceut. Sci. 9 (2006) 124–132, https://doi.org/10.7939/R3J96097M.
[36] D.R. Davies, D.E.C. Corbridge, The crystal structure of sodium triphosphate, Na5P3O10, phase II, Acta Crystallogr. 11 (1958) 315–319, https://doi.org/10.1107/s0365110x58000876.
[37] J. Cai, K.P. Mineart, X. Li, R.J. Spontak, I. Manners, H. Qiu, Hierarchical self-assembly of toroidal micelles into multidimensional nanoporous superstructures, ACS Macro Lett. 7 (2018) 1040–1045, https://doi.org/10.1021/acsmacrolett.8b00445.
[38] B. Shen, Y. Zhu, Y. Kim, X. Zhou, H. Sun, Z. Lu, M. Lee, Autonomous helical propagation of active toroids with mechanical action, Nat. Commun. 10 (2019), https://doi.org/10.1038/s41467-019-09099-9.
[39] J.Y. Jun, H.H. Nguyen, S.-Y.-R. Paik, H.S. Chun, B.-C. Kang, S. Ko, Preparation of size-controlled bovine serum albumin (BSA) nanoparticles by a modified desolvation method, Food Chem. 127 (2011) 1892–1898, https://doi.org/10.1016/j.foodchem.2011.02.040.
[40] A. Elzoghby, Helmy, Elgindy Samy, Novel ionically crosslinked casein nanoparticles for flutamide delivery: formulation, characterization, and in vivo pharmacokinetics, Int. J. Nanomed. (2013), https://doi.org/10.2147/ijn.S40674.
[41] X. Deng, M. Cao, J. Zhang, K. Hu, Z. Yin, Z. Zhou, X. Xiao, Y. Yang, W. Sheng, Y. Wu, Y. Zeng, Hyaluronic acid-chitosan nanoparticles for co-delivery of MiR-34a and doxorubicin in therapy against triple negative breast cancer, Biomaterials 35 (2014) 4333–4344, https://doi.org/10.1016/j.biomaterials.2014.02.006.
[42] M. Papi, V. Palmieri, G. Maulucci, G. Arcovito, E. Greco, G. Quintiliani, M. Fraziano, M. De Spirito, Controlled self assembly of collagen nanoparticle, J. Nanoparticle Res. 13 (2011) 6141–6147, https://doi.org/10.1007/s11051-011-0327-x.
[43] P.C. Bessa, R. Machado, S. Nürnberger, D. Dopler, A. Banerjee, A.M. Cunha, J. C. Rodríguez-Cabello, H. Redl, M. van Griensven, R.L. Reis, M. Casal, Thermoresponsive self-assembled elastin-based nanoparticles for delivery of BMPs, J. Contr. Release 142 (2010) 312–318, https://doi.org/10.1016/j.jconrel.2009.11.003.
[44] N. Dixit, K. Vaibhav, R.S. Pandey, U.K. Jain, O.P. Katare, A. Katyal, J. Madan, Improved cisplatin delivery in cervical cancer cells by utilizing folate-grafted non-aggregated gelatin nanoparticles, Biomed. Pharmacother. 69 (2015) 1–10, https://doi.org/10.1016/j.biopha.2014.10.016.
[45] M.A. Arangoa, M.A. Campanero, M.J. Renedo, G. Ponchel, J.M. Irache, Gliadin nanoparticles as carriers for the oral administration of lipophilic drugs. Relationships between bioadhesion and pharmacokinetics, Pharmaceut. Res. 18 (2001) 1521–1527, https://doi.org/10.1023/a:1013018111829.
[46] S. Dreis, F. Rothweiler, M. Michaelis, J. Cinatl, J. Kreuter, K. Langer, Preparation, characterisation and maintenance of drug efficacy of doxorubicin-loaded human serum albumin (HSA) nanoparticles, Int. J. Pharm. 341 (2007) 207–214, https://doi.org/10.1016/j.ijpharm.2007.03.036.
[47] S. Ko, S. Gunasekaran, Preparation of sub-100-nm β-lactoglobulin (BLG) nanoparticles, J. Microencapsul. 23 (2008) 887–898, https://doi.org/10.1080/02652040601035143.
[48] B.R. Sloat, M.A. Sandoval, A.M. Hau, Y. He, Z. Cui, Strong antibody responses induced by protein antigens conjugated onto the surface of lecithin-based nanoparticles, J. Contr. Release 141 (2010) 93–100, https://doi.org/10.1016/j.jconrel.2009.08.023.
[49] J. Park, S.R. Hwang, J.U. Choi, F. Alam, Y. Byun, Self-assembled nanocomplex of PEGylated protamine and heparin–suramin conjugate for accumulation at the tumor site, Int. J. Pharm. 535 (2018) 38–46, https://doi.org/10.1016/j.ijpharm.2017.10.055.
[50] A.S. Lammel, X. Hu, S.-H. Park, D.L. Kaplan, T.R. Scheibel, Controlling silk fibroin particle features for drug delivery, Biomaterials 31 (2010) 4583–4591, https://doi.org/10.1016/j.biomaterials.2010.02.024.
[51] B. Krithika, R. Preetha, Formulation of protein based inulin incorporated synbiotic nanoemulsion for enhanced stability of probiotic, Mater. Res. Express 6 (2019), https://doi.org/10.1088/2053-1591/ab4d1a.
[52] H. Chen, Q. Zhong, A novel method of preparing stable zein nanoparticle dispersions for encapsulation of peppermint oil, Food Hydrocolloids 43 (2015) 593–602, https://doi.org/10.1016/j.foodhyd.2014.07.018.
[53] R. Dougherty, K.H. Kunzelmann, Computing local thickness of 3D structures with ImageJ, Microsc. Microanal. 13 (2007), https://doi.org/10.1017/s1431927607074430.
[54] S.R. Gallagher, Digital Image Processing and Analysis with ImageJ, Current Protocols Essential Laboratory Techniques2010.
[55] R.F. Egerton, Choice of operating voltage for a transmission electron microscope, Ultramicroscopy 145 (2014) 85–93, https://doi.org/10.1016/j.ultramic.2013.10.019.
[56] P.M. Carvalho, M.R. Felício, N.C. Santos, S. Gonçalves, M.M. Domingues, Application of light scattering techniques to nanoparticle characterization and development, Front. Chem. 6 (2018), https://doi.org/10.3389/fchem.2018.00237.
[57] A.M. Etorki, M. Gao, R. Sadeghi, L.F. Maldonado-Mejia, J.L. Kokini, Effects of desolvating agent types, ratios, and temperature on size and nanostructure of nanoparticles from α-lactalbumin and ovalbumin, J. Food Sci. 81 (2016) E2511–E2520, https://doi.org/10.1111/1750-3841.13447.
[58] W. Fraunhofer, G. Winter, C. Coester, Asymmetrical flow field-flow fractionation and multiangle light scattering for analysis of gelatin nanoparticle drug carrier systems, Anal. Chem. 76 (2004) 1909–1920, https://doi.org/10.1021/ac0353031.
[59] R.J. Naftalin, M.C.R. Symons, The mechanism of sugar-dependent stabilisation of gelatin gels, Biochim. Biophys. Acta Biomembr. 352 (1974) 173–178, https://doi.org/10.1016/0005-2736(74)90188-6.
[60] V. Sokolova, G. Mekky, S.B. van der Meer, M.C. Seeds, A.J. Atala, M. Epple, Transport of ultrasmall gold nanoparticles (2 nm) across the blood-brain barrier in a six-cell brain spheroid model, Sci. Rep. 10 (2020) 18033, https://doi.org/10.1038/s41598-020-75125-2.
[61] E. Karathanasis, H.B. Frieboes, M. Wu, J. Lowengrub, P. Decuzzi, V. Cristini, A computational model for predicting nanoparticle accumulation in tumor vasculature, PLoS One 8 (2013), https://doi.org/10.1371/journal.pone.0056876.
[62] W. Yu, C. Hu, H. Gao, Intelligent size-changeable nanoparticles for enhanced tumor accumulation and deep penetration, ACS Applied Bio Materials 3 (2020) 5455–5462, https://doi.org/10.1021/acsabm.0c00917.
[63] M.J. Mitchell, M.M. Billingsley, R.M. Haley, M.E. Wechsler, N.A. Peppas, R. Langer, Engineering precision nanoparticles for drug delivery, Nat. Rev. Drug Discov. 20 (2020) 101–124, https://doi.org/10.1038/s41573-020-0090-8.
[64] H. Xu, T.Y. Ohulchanskyy, A. Yakovliev, R. Zinyuk, J. Song, L. Liu, J. Qu, Z. Yuan, Nanoliposomes Co-encapsulating CT imaging contrast agent and photosensitizer for enhanced, imaging guided photodynamic therapy of cancer, Theranostics 9 (2019) 1323–1335, https://doi.org/10.7150/thno.31079.
[65] Z. Cheng, D.L.J. Thorek, A. Tsourkas, Porous polymersomes with encapsulated Gd-labeled dendrimers as highly efficient MRI contrast agents, Adv. Funct. Mater. 19 (2009) 3753–3759, https://doi.org/10.1002/adfm.200901253.
[66] M.J. Sailor, J.-H. Park, Hybrid nanoparticles for detection and treatment of cancer, Adv. Mater. 24 (2012) 3779–3802, https://doi.org/10.1002/adma.201200653.
[67] M. Ha, J.-H. Kim, M. You, Q. Li, C. Fan, J.-M. Nam, Multicomponent plasmonic nanoparticles: from heterostructured nanoparticles to colloidal composite nanostructures, Chem. Rev. 119 (2019) 12208–12278, https://doi.org/10.1021/acs.chemrev.9b00234.
[68] N.P.B. Tan, C.H. Lee, Environment-Friendly Approach in the Synthesis of Metal/Polymeric Nanocomposite Particles and Their Catalytic Activities on the Reduction of P-Nitrophenol to P-Aminophenol, Green Chemical Processing and Synthesis2017.
[69] B. Gong, Y. Shen, H. Li, X. Li, X. Huan, J. Zhou, Y. Chen, J. Wu, W. Li, Thermo-responsive polymer encapsulated gold nanorods for single continuous wave laser-induced photodynamic/photothermal tumour therapy, J. Nanobiotechnol. 19 (2021), https://doi.org/10.1186/s12951-020-00754-8.

[70] G. Yang, Z. Xiao, H. Long, K. Ma, J. Zhang, X. Ren, J. Zhang, Assessment of the characteristics and biocompatibility of gelatin sponge scaffolds prepared by various crosslinking methods, Sci. Rep. 8 (2018), https://doi.org/10.1038/s41598-018-20006-y.

[71] S.K. Jain, Y. Gupta, A. Jain, A.R. Saxena, P. Khare, A. Jain, Mannosylated gelatin nanoparticles bearing an anti-HIV drug didanosine for site-specific delivery, Nanomed. Nanotechnol. Biol. Med. 4 (2008) 41–48, https://doi.org/10.1016/j.nano.2007.11.004.

[72] E.J. Lee, S.A. Khan, J.K. Park, K.-H. Lim, Studies on the characteristics of drug-loaded gelatin nanoparticles prepared by nanoprecipitation, Bioproc. Biosyst. Eng. 35 (2011) 297–307, https://doi.org/10.1007/s00449-011-0591-2.

[73] C. Kuttner, R.P.M. Höller, M. Quintanilla, M.J. Schnepf, M. Dulle, A. Fery, L.M. Liz-Marzán, SERS and plasmonic heating efficiency from anisotropic core/satellite superstructures, Nanoscale 11 (2019) 17655–17663, https://doi.org/10.1039/c9nr06102a.

[74] J.M. Provenzale, G.A. Silva, Uses of nanoparticles for central nervous system imaging and therapy, Am. J. Neuroradiol. 30 (2009) 1293–1301, https://doi.org/10.3174/ajnr.A1590.

[75] L. He, M. Brasino, C. Mao, S. Cho, W. Park, A.P. Goodwin, J.N. Cha, DNA-Assembled core-satellite upconverting-metal–organic framework nanoparticle superstructures for efficient photodynamic therapy, Small 13 (2017), https://doi.org/10.1002/smll.201700504.

[76] Q. Xiao, X. Zheng, W. Bu, W. Ge, S. Zhang, F. Chen, H. Xing, Q. Ren, W. Fan, K. Zhao, Y. Hua, J. Shi, A core/satellite multifunctional nanotheranostic for in vivo imaging and tumor eradication by radiation/photothermal synergistic therapy, J. Am. Chem. Soc. 135 (2013) 13041–13048, https://doi.org/10.1021/ja404985w.

[77] R.P.M. Höller, M. Dulle, S. Thomä, M. Mayer, A.M. Steiner, S. Förster, A. Fery, C. Kuttner, M. Chanana, Protein-assisted assembly of modular 3D plasmonic raspberry-like core/satellite nanoclusters: correlation of structure and optical properties, ACS Nano 10 (2016) 5740–5750, https://doi.org/10.1021/acsnano.5b07533.